

A radar survey of M- and X-class asteroids II. Summary and synthesis

Michael K. Shepard^{a,*}, Beth Ellen Clark^b, Maureen Ockert-Bell^b, Michael C. Nolan^c, Ellen S. Howell^c, Christopher Magri^d, Jon D. Giorgini^e, Lance A.M. Benner^e, Steven J. Ostro^e, Alan W. Harris^f, Brian D. Warner^g, Robert D. Stephens^h, Michael Muellerⁱ

^aBloomsburg University, 400 E. Second St., Bloomsburg, PA 17815, USA

^bIthaca College, 267 Center for Natural Sciences, Ithaca, NY 14853, USA

^cNAIC/Arecibo Observatory, HC 3 Box 53995, Arecibo, PR 00612, USA

^dUniversity of Maine at Farmington, 173 High Street, Preble Hall, ME 04938, USA

^eJet Propulsion Laboratory, Pasadena, CA 91109, USA

^fSpace Science Institute, La Canada, CA 91011-3364, USA

^gPalmer Divide Observatory/Space Science Institute, Colorado Springs, CO 80908, USA

^hSantana Observatory, 11355 Mount Johnson Court, Rancho Cucamonga, CA 91737, USA

ⁱObservatoire de la Côte d'Azur, B.P. 4229, 06304 NICE Cedex 4, France

ARTICLE INFO

Article history:

Received 21 September 2009

Revised 12 January 2010

Accepted 14 January 2010

Available online 22 January 2010

Keywords:

Asteroids

Asteroids, Composition

ABSTRACT

Using the S-band radar at Arecibo Observatory, we observed six new M-class main-belt asteroids (MBAs), and re-observed one, bringing the total number of Tholen M-class asteroids observed with radar to 19. The mean radar albedo for all our targets is $\bar{\sigma}_{OC} = 0.28 \pm 0.13$, significantly higher than the mean radar albedo of every other class (Magri, C., Nolan, M.C., Ostro, S.J., Giorgini, J.D. [2007]. *Icarus* 186, 126–151). Seven of these objects (Asteroids 16 Psyche, 129 Antigone, 216 Kleopatra, 347 Pariana, 758 Mancunia, 779 Nina, 785 Zwetana) have radar albedos indicative of a very high metal content (mean $\bar{\sigma}_{OC} = 0.41 \pm 0.13$), and consistent with a remnant iron/nickel core interpretation (irons) or exotic high metal meteorite types such as CB. We propose designating these high radar albedo objects as Mm. Two asteroids, 110 Lydia and 678 Fredegundis, have more moderate radar albedos (mean $\bar{\sigma}_{OC} = 0.22$), but exhibit high values ($\bar{\sigma}_{OC} \sim 0.35$) at some rotation phases suggesting a significant metal content. The remaining 10 objects have moderate radar albedos ($\bar{\sigma}_{OC} = 0.20 \pm 0.06$) at all rotation phases. Most of our targets have visible/near-infrared spectra (Hardersen, P.S., Gaffey, M.J., Abell, P.A. [2005]. *Icarus* 175, 141–158; Fornasier, S., Clark, B.E., Dotto, E., Migliorini, A., Ockert-Bell, M., Barucci, M.A. [2009]. *Icarus*, submitted for publication) that indicate the presence of at least some silicate phases. All of the non-Mm asteroids show a positive correlation between visual and radar albedo but the reasons for this are not clear. All of the higher radar albedo targets (the 7 Mm asteroids, Lydia, and Fredegundis) show moderate to large variations in radar albedo with rotation phase. We suggest that their high radar reflectivity exaggerates irregularities in the asteroid shape to cause this behavior. One-third of our targets show evidence for asteroid-scale concavities or bifurcation. Based on all the evidence available, we suggest that most Tholen M-class asteroids are not remnant iron cores or enstatite chondrites, but rather collisional composites of silicates and irons with compositions more analogous to stony-iron meteorites and high-iron carbonaceous chondrites.

© 2010 Elsevier Inc. All rights reserved.

1. Part I. Observations of six new M-class asteroids

1.1. Introduction

The Tholen (1984) X-class asteroids are defined by featureless spectra with red-slopes and an unknown visual albedo. The Bus

X classification is similar (Bus and Binzel, 2002). Asteroids with these spectral characteristics and visual albedos in the range ~ 0.10 – 0.30 are classified as Tholen M-class. Historically, M-class asteroids were thought to be the denuded metallic cores of disrupted parent bodies or possibly enstatite chondrites (Chapman and Salisbury, 1973; Gaffey, 1976; Gaffey and McCord, 1979; Bell et al., 1989; Cloutis et al., 1990). However, a number of studies have uncovered subtle spectral features evident in the M-class asteroids, some of which are inconsistent with metallic compositions (Clark et al., 2004; Hardersen et al., 2005). Others have dis-

* Corresponding author. Address: Dept. of Geography and Geosciences, Bloomsburg University of Pennsylvania, 400 E. Second St., Bloomsburg, PA 17815, USA. Fax: +1 570 389 3028.

E-mail address: mshepard@bloomu.edu (M.K. Shepard).

covered evidence of 3 μm spectral features and attributed them to hydrated minerals (Jones et al., 1990; Rivkin et al., 1995, 2000) although that interpretation is still debated (Gaffey et al., 2002). M-class asteroids with this latter characteristic are referred to as W-class by Rivkin et al. (2000) and are also considered to be inconsistent with the metallic core or enstatite chondrite interpretation. Viable meteorite candidate analogs for the M-class include iron meteorites, enstatite chondrites, stony-irons (including mesosiderites, pallasites, and ungrouped members), CH/CB meteorites, and carbonaceous chondrites (CI and CM) (Chapman and Salisbury, 1973; Gaffey, 1976; Gaffey and McCord, 1979; Bell et al., 1989; Cloutis et al., 1990; Gaffey et al., 1993; Vilas, 1994; Rivkin et al., 2000; Hardersen et al., 2005; Vernazza et al., 2009). Of these, only the carbonaceous chondrites and CH/CB may contain hydrated phases in meteorite samples.

Because of absent, subtle, or ambiguous spectral information, radar is often a better tool for identifying metallic content in asteroids. Iron is several times denser than rock-forming silicates and, since radar reflectivity depends primarily upon near-surface bulk density (Ostro et al., 1985), an asteroid composed primarily of iron will have a significantly higher radar reflectivity than one composed of silicates. Since 2004, we have surveyed 19 M-class asteroids using the S-band radar at the Arecibo Observatory in Puerto Rico. This sample represents approximately one-third of the known M-class asteroids (Belskaya and Lagerkvist, 1996). Because echo power decreases with the fourth power of distance, Arecibo is the only radar system with sufficient power and sensitivity to systematically probe the main-belt. Where possible, we enlisted the NASA Infrared Telescope Facility (IRTF) to complement the radar observations with near- and thermal-infrared observations. Those results are described in companion papers by Ockert-Bell et al. (2008, 2010) and Mueller et al. (2010).

The paper is outlined as follows. In Part I, we briefly discuss the conventions and equations used in our radar analysis and describe the results for seven new radar data sets. In Part II, we develop a heuristic model for linking the observed radar albedo to an asteroid's near-surface bulk density, list and describe the suggested meteorite analogs for M-class asteroids, and use this model and our observations to constrain the best meteoritic analogs for these objects. We discuss other characteristics of our sample and, assuming our sample to be representative of the larger population, suggest a new interpretation for the M-class asteroids.

1.2. Conventions and equations

In this section we review the conventions and equations that describe the relationship between radar, thermal, and optical measurements and the physical properties of these asteroids used in this paper.

1.2.1. Asteroid shape, size, rotation period, and optical properties

To place constraints on a target's diameter, we use the following relationship between effective diameter (D_{eff} , in kilometers), visual albedo (p_v), and absolute magnitude (H) (Pravec and Harris, 2007):

$$\log D_{\text{eff}} \text{ (km)} = 3.1235 - 0.2H - 0.5 \log p_v. \quad (1)$$

The effective diameter D_{eff} is the diameter of a sphere with the same projected area as the asteroid.

We assume each asteroid can be modeled as a triaxial ellipsoid with long, intermediate, and short axes of 'a', 'b', and 'c', respectively. The c-axis is assumed to be the rotation axis. We characterize the shape of the ellipsoid with the ratios of these axes: a/b and a/c or b/c .

For diameters determined by thermal analysis of our data or IRAS data (Tedesco et al., 2002), we adopt uncertainties of at least $\pm 10\%$ to take into account both the (smaller) random uncertainties

quoted for each diameter and potentially larger systematic uncertainties (Lebofsky, 1989).

Unless otherwise noted, all rotation periods and lightcurve amplitudes are taken from the asteroid lightcurve database and references therein (Warner et al., 2009a). Uncertainties in the rotation periods are on the order of the last significant digit.

1.2.2. Radar analysis

Each observing cycle or "run" consisted of transmission of a circularly polarized 2380 MHz (12.6 cm) signal for the round-trip light travel time to the target, followed by reception of echoes for a similar duration in the opposite (OC) and same (SC) senses of circular polarization as transmitted. We measured the radar cross-sections of our targets (in km^2) σ_{OC} and σ_{SC} , by integrating the continuous wave (CW) power spectra. These are equivalent to the cross-sectional areas of a smooth, metallic sphere (a perfect reflector) that would generate the observed echo power when viewed at the same distance.

For an asteroid observed at S-band (2380-MHz), its plane-of-sky extent (in kilometers) normal to the apparent spin vector at rotation phase φ , $D(\varphi)$, is related to the instantaneous bandwidth B (in Hertz) of the radar echo (due to the apparent rotation), the target's physical properties, and its orientation by

$$D(\varphi) = \frac{PB(\varphi)}{27.7 \cos \delta}, \quad (2)$$

where P is the apparent (synodic) rotation period in hours and δ is the sub-radar latitude. For each target we estimate the minimum bandwidth and the corresponding lower bound on the maximum pole-on breadth, D_{max} , using Eq. (2). Our experience with asteroids of weak to moderate signal-to-noise ratio (SNR) (optimally filtered sum SNR ≤ 20 or so) suggests that we can obtain a reasonable estimate of the bandwidth using the points where echo power drops to zero standard deviations (zero-crossing or $B_{2\sigma}$) after smoothing in frequency to boost the SNR. For signals with higher SNR, we often adopt the points at which the echo drops below two standard deviations of noise ($B_{2\sigma}$). Uncertainties are typically based on the frequency resolution of the spectrum. In a few instances, we adopt a bandwidth, B , which is somewhat narrower based upon the waveform behavior, and adopt conservative uncertainties. We get a sense for the goodness of a bandwidth estimate by comparing it to the bandwidth of the optimal filter for maximizing the signal-to-noise ratio, referred to as the "effective frequency resolution", or "effective resolution." In general, this is narrower than the estimated bandwidth, but it should be comparable.

The circular polarization ratio, μ_c , is defined to be the ratio of the SC and OC echo power:

$$\mu_c = \frac{\sigma_{\text{SC}}}{\sigma_{\text{OC}}}. \quad (3)$$

Values larger than zero are thought to be caused by wavelength-scale near-surface (~ 1 m depth for 12 cm wavelength) roughness and inhomogeneities and/or subsurface or multiple scattering. Smooth surfaces have polarization ratios approaching 0.0, while some extremely rough surfaces have values near or at unity (Ostro et al., 2002; Benner et al., 2008).

The OC radar albedo, $\hat{\sigma}_{\text{OC}}$, of an asteroid is defined to be the ratio of its OC radar cross-section (σ_{OC}) to its cross-sectional area,

$$\hat{\sigma}_{\text{OC}} = \frac{4\sigma_{\text{OC}}}{\pi D_{\text{eff}}^2}. \quad (4)$$

$\hat{\sigma}_{\text{OC}}$ can vary with rotation and aspect. Published MBA radar albedos vary from a low of 0.039 for the CP-class main-belt asteroid (MBA) 247 Eukrate (Magri et al., 2007) to a maximum of 0.6 for the M-class 216 Kleopatra (Ostro et al., 2000).

Uncertainties in our estimates of absolute radar cross-section are usually $\pm 25\%$ and are based on estimates of systematic uncertainties in transmitted power and calibration. Because systematic uncertainties are nearly the same for both polarization senses, uncertainties in circular polarization ratio are dominated by receiver thermal noise. Unless otherwise stated, our quoted uncertainties for random errors are one-standard deviation.

1.3. New radar observations of M-class MBAs

In this section, we summarize our recent radar observations of six new and one repeat M-class MBAs. Observing circumstances for all targets are given in Table 1, and Table 2 lists the measured radar properties of each target.

1.3.1. 110 Lydia

Lydia has an IRAS-derived diameter of $D_{\text{eff}} = 86 \pm 9$ km, an optical albedo of $p_v = 0.18 \pm 0.01$ (Tedesco et al., 2002), and rotational period of $P = 10.92580$ h (Durech et al., 2007). Originally classified as a Tholen X-type, its optical albedo places it in the Tholen M-class.

Rivkin et al. (2000) observed a $3 \mu\text{m}$ absorption feature attributed to hydration, considered to be inconsistent with a metallic core interpretation, and classified Lydia as a W.

Optical polarimetry (Lupishko and Belskaya, 1989) suggests that the surface of Lydia contains a significant silicate component. Visible and near-IR spectra of Lydia support this interpretation with evidence for the presence of iron-poor orthopyroxenes (Harden et al., 2005; Ockert-Bell et al., 2010).

Using 26 lightcurves from four oppositions, Durech et al. (2007) derive a spin and convex shape model for Lydia. They report two possible poles at (λ, β) $(331^\circ, -61^\circ)$ and $(149^\circ, -55^\circ)$ with uncertainties of approximately $\pm 10^\circ$. Their shape model has aspect ratios of $a/b \sim 1.1$, consistent with Lydia's low lightcurve amplitude of < 0.3 mag., and $a/c \sim 1.5$. Using additional lightcurves from the November 2008 opposition, Warner et al. (2009b) revised the Durech et al. model, finding possible poles at $(345^\circ, -51^\circ)$ and $(164^\circ, -43^\circ)$ with a radial uncertainty of $\sim 15^\circ$; their shape model is also not as flattened along the c -axis, with $a/c \sim 1.2$. Based on our review of all previous lightcurves, we conclude that, while there is good evidence that $a/b \sim 1.1$, the a/c ratio cannot be reliably constrained from the lightcurves alone. For the analysis here, we adopt the more conservative aspect ratios, $a/b = 1.1$ and $a/c = 1.2$, giving $D_{\text{max}} = 1.1 * D_{\text{eff}}$.

We observed Lydia at Arecibo from 8 to 12 November 2008 (Table 1) and obtained nine runs with a total SNR of 10 at an effective frequency resolution of 155 Hz (Fig. 1, Table 2). For the weighted sum of all echoes, we measured a bandwidth $B_{\text{ZC}} = 190 \pm 30$ Hz, an OC cross-section $\sigma_{\text{OC}} = 1230 \pm 300 \text{ km}^2$, and polarization ratio

$\mu_c = 0.02 \pm 0.02$; the latter is indicative of a smooth near-surface. As seen in Fig. 2, most of the individual echoes were weak with SNRs ranging from ~ 2 to 5. The exception, run #5 on 10 November is more than twice as strong with SNR ~ 11 . This suggests: (1) a compositional variation and (2) a large-scale structural differences with rotation phase, or some combination of these. The waveform of this run shows evidence for a large concavity or bifurcation.

To help better constrain Lydia's size and spin state, we also observed Lydia in the thermal infrared using the Mid-IR Spectrometer and Imager (MIRSI) on the NASA IRTF. These observations were made simultaneously with the radar observations on 9 November. From those data, Mueller et al. (2010) estimate Lydia's diameter to be $D_{\text{eff}} = 97 \pm 15$ km, larger than the IRAS diameter of 86 km, but consistent to within the uncertainties.

To explore the range of diameter and spin-pole solutions, we calculated the χ^2 of every possible pole position for a given maximum diameter (D_{max}) consistent with our observed radar bandwidth. These values were then contoured on two-dimensional ecliptic-coordinate $(\lambda-\beta)$ plots. Fig. 3 shows contours of χ^2 consistent with the radar bandwidth and $D_{\text{max}} = 95$ km. The position of Lydia at the time of our radar observations is noted by the bold asterisk and the χ^2 contours are concentric about it. Since our solutions are north-south ambiguous (i.e. we do not know if our sub-radar latitude was in the northern or southern hemisphere), we also plot the alternative or mirror solution contours; these are concentric about the lighter asterisk. To be consistent with the radar data, the published spin-poles should be within or near the 1-sigma χ^2 contours. Within uncertainties, both sets of pole solutions fall within the minima troughs bounded by the 1-sigma χ^2 contours. We explored a range of other diameters and, including spin-pole uncertainties, find that $75 \text{ km} \leq D_{\text{max}} < 100 \text{ km}$.

Although smaller D_{max} are more consistent with the published poles, they are less consistent with the reported thermal size estimates. Because the thermal sizes are based on observed cross-sectional area and are similar to our radar constrained D_{max} , we find that Lydia cannot be very polar-flattened. This is consistent with the axial ratios and shape model discussed earlier. Based on all the data at our disposal, we estimate $D_{\text{max}} = 98 \pm 8$ km and $D_{\text{eff}} = 89 \pm 9$ km. Our data are also marginally more consistent with the spin-pole solutions at longitudes near 340° . Warner et al. (2009b) also found these solutions to be slightly preferred in their lightcurve inversion.

Our composite diameter and observed radar cross-section give a radar albedo $\hat{\sigma}_{\text{OC}} = 0.20 \pm 0.05$. This value is generally inconsistent with a metallic interpretation. However, if we estimate the radar albedo based on run #5 only, we obtain $\hat{\sigma}_{\text{OC}} = 0.38 \pm 0.05$, which suggests a significant metal content at that orientation.

Table 1
Observing circumstances.

Target	Date	RA ($^\circ$)	Dec. ($^\circ$)	Elon. ($^\circ$)	Elat. ($^\circ$)	Dist. AU	Runs	OC SNR	Observation window
110 Lydia	2008 November 8–12	100	27	99	4	2.02	9	10	06:30–09:00
135 Hertha	2008 November 11	48	22	52	4	1.31	2	17	03:00–05:00
347 Pariana	2006 April 11–23	205	10	200	19	1.26	6	27	02:30–06:00
497 Iva	2008 November 7–12	65	28	67	7	1.23	5	10	04:00–07:00
678 Fredegundis	2007 January 10–17	113	20	112	−2	1.30	10	15	02:45–06:00
771 Libera	2008 November 6–10	68	12	68	−10	1.10	7	8	04:15–07:00
779 Nina	2008 November 9–12	72	37	75	14	1.64	3	12	05:15–06:30

Transmitter power was between 600 and 700 kW for all targets.

RA, Dec. indicate the asteroid position (J2000) at center of observation window.

Elon. and Elat. indicate the asteroid position in ecliptic-coordinates (longitude and latitude).

Dist. is the Earth–asteroid distance.

Runs is the number of transmit–receive cycles.

OC SNR is the SNR of the optimally filtered weighted sum of all OC runs.

Observation window gives the UTC window during which we received data.

Table 2
CW radar properties of individual targets.

Asteroid	Date	Time UT	SNR	φ (°)	B (Hz)	σ_{oc} (km ²)	μ_c
110 Lydia	2008 November 08	7:29	2	0	–	–	–
	2008 November 08	8:29	4	33	170	1480	0.25
	2008 November 09	7:26	5	69	185	1490	0.00
	2008 November 09	8:28	3	103	205	1110	0.40
	2008 November 10	7:20	11	137	150	2390	0.00
	2008 November 10	8:20	3	169	–	–	–
	2008 November 11	7:16	5	205	140	1310	0.19
	2008 November 11	8:18	3	239	120	800	0.14
	2008 November 12	7:11	4	273	250	1190	0.00
	Sum of dates	–	10	–	190 ± 30	1230 ± 300	0.02 ± 0.02
135 Hertha	2008 November 11	04:09	10	0	150	790	0.08
	2008 November 11	04:54	14	32	150	980	0.06
	Sum of dates	–	17	–	180 ± 40	890 ± 230	0.07 ± 0.05
347 Pariana	2008 April 11	4:11	11	0	135	510	0.00
	2008 April 11	4:56	18	67	200	990	0.04
	2008 April 11	5:46	11	141	150	630	0.08
	2008 April 12	4:07	14	326	185	775	0.00
	2008 April 23	3:15	7	300	250	565	0.05
	2008 April 23	3:58	9	2	125	480	0.11
	Sum of dates	–	27	–	170 ± 30	730	0.03 ± 0.03
497 Iva	2008 November 7–12	–	10	–	240 ± 50	300 ± 80	0.11 ± 0.03
678 Fredegundis	2008 January 10	4:22	7	0	80	280	0.00
	2008 January 10	5:05	4	22	85	185	0.00
	2008 January 10	5:48	5	45	83	190	0.31
	2008 January 11	3:59	5	11	100	270	0.00
	2008 January 11	4:42	5	34	75	230	0.11
	2008 January 11	5:25	9	56	95	460	0.00
	2008 January 12	4:55	8	64	100	340	0.05
	2008 January 12	5:38	7	86	50	215	0.00
	2008 January 17	4:09	2	158	60	70	0.24
	2008 January 17	4:52	6	180	60	205	0.45
	Sum of dates	–	15	–	100 ± 20	240 ± 60	0.03 ± 0.06
771 Libera	2008 November 6–10	–	8	–	135 ± 40	120 ± 30	0.4 ± 0.1
779 Nina	2008 November 9	6:21	5	0	110	1010	0.00
	2008 November 11	6:07	12	97	155	2280	0.23
	2008 November 12	6:00	4	7	105	615	0.43
	Sum November 9 + 12	–	5	4	135 ± 30	735	0.00 ± 0.10
	Sum of dates	–	11	–	135 ± 20	1205 ± 300	0.16 ± 0.08

Values in the “sum of dates” are based on the weighted sum of all runs. Time and date are the mid-epochs of acquisition (UT). φ is rotation phase starting arbitrarily from the receipt of the first run (°). B is zero-crossing bandwidth (Hz) for data smoothed in frequency (see text for specifics). σ_{oc} is the OC radar cross-section (km²), and μ_c is the polarization ratio. Uncertainties in radar cross-section are 25%.

1.3.2. 135 Hertha

Hertha has an IRAS-derived diameter of $D_{eff} = 79 \pm 8$ km, an optical albedo of $p_v = 0.14 \pm 0.01$ (Tedesco et al., 2002), and period $P = 8.4006$ h (Torppa et al., 2003). Hertha is one of the larger members of the Nysa family and has been interpreted as the remnant core of a disrupted parent body which produced both Nysa (an E-class object) and Hertha (Zellner et al., 1977). Rivkin et al. (2000) observed a 3 μ m absorption feature that they attributed to hydration and placed Hertha in their W-class. Cellino et al. (2001) suggested that Hertha may be an interloper to the Nysa family and also argued against the remnant core interpretation. Cellino et al. (2003) observed Hertha using speckle interferometry and estimated $D_{eff} = 83 \pm 12$ km from the projected ellipsoid they observed.

Using lightcurves from eight apparitions, Torppa et al. (2003) derive a shape for Hertha with axis ratios $a/b = 1.1$ and $b/c = 1.5$ and report two possible poles: $(\lambda, \beta) = (96^\circ, +58^\circ)$ and $(274^\circ, +53^\circ)$ with radial uncertainties of $\pm 5^\circ$. Durech, expanding upon this work, finds similar shapes and poles of $(96^\circ, 55^\circ)$ or $(273^\circ, 52^\circ)$ with similar uncertainties (<http://astro.troja.mff.cuni.cz/~projects/asteroids3D/web.php>).

We observed Hertha in the thermal infrared using the MIRS1 at the IRTF on 9 November. From those data, we estimate Hertha’s diameter to be $D_{eff} = 91 \pm 14$ km, larger than the IRAS diameter, but consistent within the uncertainties (Mueller et al., 2010).

On 11 December 2008 a well-coordinated campaign of amateur and professional astronomers observed a stellar occultation by Hertha (Timerson et al., 2009). The silhouette was consistent with that expected from the Durech convex shape model and the pole at $(273^\circ, 52^\circ)$; the maximum axis of the best fit ellipsoid was 101 km, and the maximum length of the irregular shape was ~ 97 km. From these direct measurements, we adopt $D_{max} = 100$ km. Given that the occultation profile matched the Durech shape model, we adopt their shape and the occultation-based size, giving $D_{eff} = 77 \pm 7$ km.

Shepard et al. (2008a) observed Hertha at Arecibo in September and October 2004, and obtained four CW runs with a total SNR of 48. The bandwidth of those observations was $B_{2\sigma} = 225 \pm 50$ Hz and the OC cross-section was $\sigma_{oc} = 810 \pm 250$ km², giving a radar albedo estimate of 0.18 ± 0.06 .

We observed Hertha again on 11 November 2008 (Table 1) and obtained two runs with a total SNR of 17 at an effective frequency resolution of 145 Hz. We measured $B_{2\sigma} = 180 \pm 40$ Hz and radar

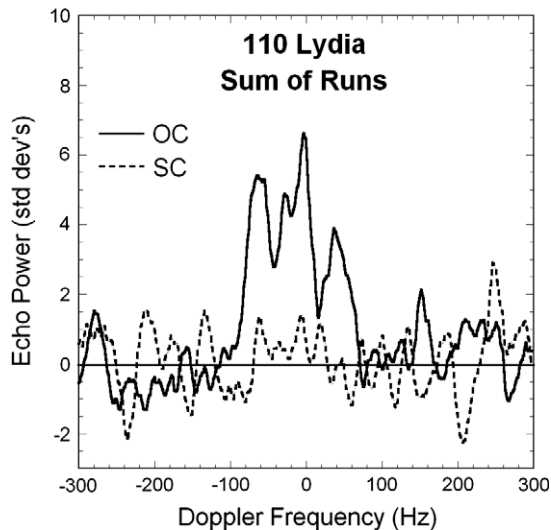


Fig. 1. CW spectrum of Lydia, consisting of the sum of all nine runs, smoothed to 20 Hz effective frequency resolution.

cross-section of $\sigma_{OC} = 890 \pm 230 \text{ km}^2$ (Fig. 4, Table 2), consistent with our previous measurement. Adopting the occultation-derived diameter of 77 km, our OC cross-sections gives a radar albedo $\hat{\sigma}_{OC} = 0.18 \pm 0.05$, consistent with our previous estimate and confirming that Hertha is probably not a remnant metallic core fragment. We measured a circular polarization ratio of $\mu_c = 0.10 \pm 0.03$, suggesting a moderately smooth near-surface.

1.3.3. 347 Pariana

Pariana's has an IRAS-derived diameter of $D_{eff} = 51 \pm 5 \text{ km}$, an optical albedo of $p_v = 0.18$ (Tedesco et al., 2002), and a rotation period of $P = 4.0529 \text{ h}$. From the analysis of many lightcurves, Tunglag et al. (2003) estimate its aspect ratios to be $a/b = 1.36$ and $b/c = 1.3$ and its rotational pole to be within approximately 10° of (λ, β) ($30^\circ, 12^\circ$).

We observed Pariana at Arecibo between 11 and 23 April 2008 (Table 1), obtaining six (6) runs with a total SNR of 27 at an effective frequency resolution of 145 Hz. The weighted sum of all runs has a bandwidth $B = 170 \pm 30 \text{ Hz}$ (Fig. 5, Table 2). Assuming the IRAS diameter and published rotational period, we expect a bandwidth of $\sim 350 \text{ Hz}$ for an equatorial view. Our observed bandwidth therefore suggests a sub-radar latitude of $\pm 60^\circ$. Given Pariana's sky position at the time of our observations (λ, β) ($200^\circ, 19^\circ$), Tunglag et al.'s pole predicts $\delta = -57^\circ$; our observations are therefore consistent with the published size, rotation period, and pole. We measured a total OC cross-section of $\sigma_{OC} = 730 \pm 180 \text{ km}^2$, leading to a radar albedo estimate $\hat{\sigma}_{OC} = 0.36 \pm 0.09$. We measured a polarization ratio $\mu_c = 0.05 \pm 0.03$, indicative of a smooth near-surface.

Our individual runs were of sufficient SNR to investigate Pariana's rotationally resolved properties (Fig. 6). We measured OC cross-sections ranging from a low of 480 km^2 to a high of 990 km^2 , a factor of two in variation. This is significantly greater than the 1.4 variation in physical cross-section suggested by the Tunglag et al. model. This behavior is similar to the other high radar albedo targets we have measured (Shepard et al., 2008a). Pariana's radar bandwidth also varies by a factor of two, and is higher than expected from the Tunglag shape model. Pariana may be more elongate than indicated by that model, but it is also possible that some of this variation may be due to the relatively low SNR of individual runs.

1.3.4. 497 Iva

Iva's diameter and optical albedo are uncertain. From the TRIAD data set, Morrison (1977) report a radiometric diameter

$D_{eff} = 31 \pm 6 \text{ km}$ and $p_v = 0.18 \pm 0.04$. A single IRAS observation was later reported, giving $D_{eff} = 45.3 \pm 2.5 \text{ km}$ and $p_v = 0.085 \pm 0.010$ (Tedesco, 1989). Lightcurves give a rotation period of $P = 4.62 \text{ h}$ and amplitudes of 0.38–0.50 (Warner et al., 2009a), suggesting a moderately elongate object ($a/b \sim 1.5$). Birlan et al. (2007) report visible and NIR spectra of Iva which are consistent with RELAB spectra of metal meteorites.

We observed Iva between 7 and 12 November 2008 at Arecibo and simultaneously at the IRTF in the thermal infrared on 8 November (Table 1). A preliminary analysis of the thermal data indicates a diameter of $46 \pm 10 \text{ km}$, but the rotational aspect is incomplete and unconstrained (Mueller et al., 2010).

Our radar observations consist of five runs with a total SNR of 10 at an effective frequency of 240 Hz (Table 2). The SNR per run was too low to conduct a rotationally resolved analysis. Based on the weighted sum of all runs, we estimate $B_{ZC} = 240 \pm 50 \text{ Hz}$. This bandwidth is consistent with $D_{max} \geq 40 \text{ km}$ (Fig. 7). Given these observations and the previously noted disparity in reported sizes, we adopt $D_{eff} = 40 \pm 8 \text{ km}$. Using an absolute magnitude $H = 9.87$ (Harris and Young, 1983), we estimate $p_v = 0.13 \pm 0.03$. We measured a total OC cross-section of $\sigma_{OC} = 300 \pm 80 \text{ km}^2$, leading to a radar albedo estimate $\hat{\sigma}_{OC} = 0.24 \pm 0.08$ which is inconsistent with a metallic core interpretation. We measured a polarization ratio $\mu_c = 0.11 \pm 0.03$, indicative of a moderately smooth near-surface.

1.3.5. 678 Fredegundis

Fredegundis has an IRAS-derived diameter of $D_{eff} = 42 \pm 4 \text{ km}$, an optical albedo of $p_v = 0.25 \pm 0.03$ (Tedesco et al., 2002), and a rotational period of $P = 11.6201 \text{ h}$ (Stephens et al., 2008). Classified as an X in the Bus system, its optical albedo places it in the Tholen M-class.

We observed Fredegundis at Arecibo between 10 and 17 January 2008 (Table 1), obtaining 10 runs with a total SNR of 15 at an effective frequency resolution of 85 Hz (Table 2, Fig. 8). Because its rotation period is about half of Earth's, we obtained coverage of only \sim half of its rotation. Based on the weighted sum of all runs, we estimate $B_{ZC} = 100 \pm 20 \text{ Hz}$ (Table 2). This bandwidth implies $D_{max} \geq 42 \text{ km}$, consistent with the IRAS diameter and an equatorial aspect. We measured a total OC cross-section of $\sigma_{OC} = 240 \pm 60 \text{ km}^2$, leading to a radar albedo estimate $\hat{\sigma}_{OC} = 0.18 \pm 0.05$ which is inconsistent with a metallic core interpretation. We measured a polarization ratio $\mu_c = 0.03 \pm 0.06$ which is indicative of a very smooth near-surface.

The SNR for individual runs of Fredegundis was often low, but sufficient to look for rotational variations (Fig. 9). Bandwidths varied by a factor of two suggesting modest to significant elongation, but the low SNR of some individual runs may be partially responsible for this observation. The radar cross-section varies considerably from run to run, with a highest measurement of $\sigma_{OC} = 460 \pm 120 \text{ km}^2$, about twice as high as the mean. Adopting the IRAS diameter gives a radar albedo of $\hat{\sigma}_{OC} = 0.35 \pm 0.09$ at that rotation phase, consistent with a dense regolith and significant metal content.

Two of the runs, taken on two different days at comparable rotation phases, show strongly bifurcated echoes which are evidence for a large concavity, a contact binary (twin-lobed shape), or possibly a true binary. To explore this object further, two of us (BW, RS) obtained a series of lightcurves over the weeks after the radar observations (Stephens et al., 2008). The lightcurve has a total amplitude of $\sim 0.3 \text{ mag.}$, suggesting a modest aspect ratio of $a/b \sim 1.3$. The lightcurves are consistent with a bifurcated or twin-lobed object if the larger lobe is two or more times the diameter of the smaller lobe (Stephens et al., 2008). Future shape modeling of the joint lightcurve/radar data sets may help better constrain its true nature.

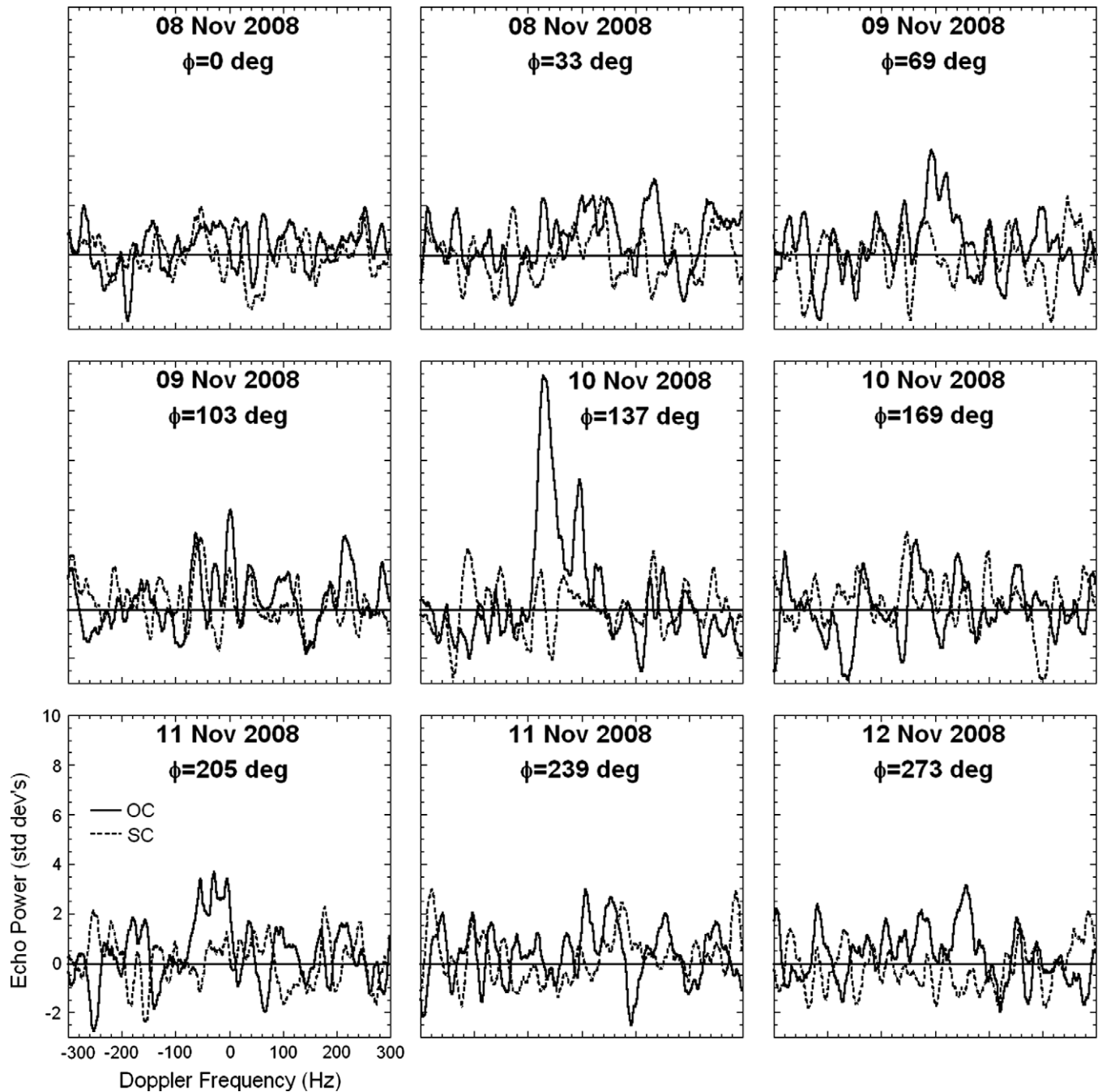


Fig. 2. Individual CW spectra of Lydia, each smoothed to 20 Hz effective frequency and labeled with the rotation phase (ϕ , arbitrarily set to 0 for the first run).

1.3.6. 771 Libera

Libera has an IRAS-derived diameter of $D_{\text{eff}} = 29 \pm 3$ km, an optical albedo of $p_v = 0.13 \pm 0.01$ (Tedesco et al., 2002), and a rotation period of $P = 5.892$ h. Classified as an X in the Tholen and Bus systems, its optical albedo places it in the Tholen M-class.

We observed 771 Libera between 6 and 10 November 2008 (Table 1), obtaining seven (7) runs with a total SNR of eight at an effective frequency resolution of 135 Hz (Fig. 10, Table 2). Our individual runs did not have sufficient SNR for rotational analysis. Based on the weighted sum of all runs, we estimate $B_{\text{ZC}} = 135 \pm 40$ Hz (Table 2) and $D_{\text{max}} \geq 29$ km. This is consistent with the IRAS diameter and an equatorial aspect. We measured a total OC cross-section of $\sigma_{\text{OC}} = 120 \pm 30$ km², giving a radar albedo estimate $\bar{\sigma}_{\text{OC}} = 0.17 \pm 0.04$ which is inconsistent with a remnant metal core.

We measured a polarization ratio $\mu_c = 0.37 \pm 0.12$, the fourth highest measured (of ~ 100 targets) for any MBA (Magri et al., 2007; Shepard et al., 2008b) and indicative of a very rough near-surface.

1.3.7. 779 Nina

Nina has an IRAS-derived diameter of $D_{\text{eff}} = 77 \pm 8$ km, an optical albedo of $p_v = 0.14 \pm 0.02$ (Tedesco et al., 2002), and a rotation period of $P = 11.186$ h. Classified as an X in the Bus system, its optical albedo places it in the Tholen M-class.

We observed Nina on November 9, 11, and 12, 2008 (Table 1). Because of its distance and position, we were only able to get one run per night for a total of three runs. The runs on November 9 and 12 were at essentially the same rotational phase, arbitrarily set to 0°, and on those nights the target was very weak. Summing

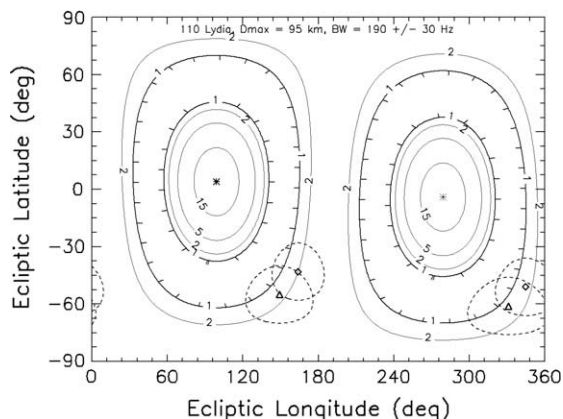


Fig. 3. χ^2 contour plot of pole solutions for Lydia assuming $D_{max} = 95$ km, the radar bandwidth (190 Hz), and its sky position at the time of the radar observations (the sky position is shown by a bold asterisk). The antipodal ambiguous solutions are centered on the lighter asterisk. Triangles are poles according to Torppa et al. (2003) and modified by Durech (see text for details); diamonds are poles from Warner et al. (2009a,b). Dashed lines around each pole indicate 15° radial uncertainties.

those two runs gives an SNR of five at an effective frequency of 120 Hz (Fig. 11). We measured $B_{ZC} = 135 \pm 30$ Hz and a total OC cross-section of $\sigma_{OC} = 735 \pm 190$ km², leading to a radar albedo estimate $\hat{\sigma}_{OC} = 0.16 \pm 0.04$ (Table 2). We measured a polarization ratio $\mu_c = 0.0 \pm 0.10$, indicative of a very smooth near-surface.

In contrast to the runs above, the run on November 11 had a strong echo with SNR of 12, also at an effective frequency of 120 Hz (Fig. 11). The rotation phase for this run was 90° away from the other two runs. The echo waveform is strongly bifurcated, suggesting either a large concavity or possibly a contact binary structure. We were unable to get another run at a rotation phase of 270° to check this. We measured $B_{ZC} = 135 \pm 20$ Hz and an OC cross-section of $\sigma_{OC} = 2280 \pm 570$ km², leading to a radar albedo estimate $\hat{\sigma}_{OC} = 0.50 \pm 0.12$ at that rotation phase and consistent with a high metal content. We measured a polarization ratio $\mu_c = 0.25 \pm 0.07$, indicative of a rough near-surface. However, if there is a significant indentation or bifurcation, the surface could be smooth and the high SC echo (and associated polarization ratio) could be caused by a double-bounce from one side or lobe to the other before returning to Earth.

The bandwidths measured at the perpendicular rotation phases are similar and suggest Nina is not very elongate. Lightcurves measured by Harris et al. (1992) show a $\Delta mag. \sim 0.25$, indicating a modest elongation. Our observations constrain Nina's maximum diameter to be $D_{max} \geq 55$ km. Adopting the IRAS-derived diameter, we estimate that we observed Nina at a sub-radar latitude $|\delta| = 45^\circ \pm 15^\circ$.

2. Part II. Synthesis of M-class asteroid properties

2.1. Radar model

A major goal of this work is to determine the best meteoritic analog(s) for M-class asteroids. To do this, we develop a heuristic model based on what is known about the radar reflectivity of powdered materials and what is believed to be true for MBA surfaces and compositions. This model will estimate surface bulk density from radar albedo (or vice versa), and allow us to compare our estimated surface densities to those of meteorite analogs (Section 2.2, below).

2.1.1. Model assumptions

We assume that all the larger main-belt asteroids have a developed surface regolith that is at least several meters in depth so that

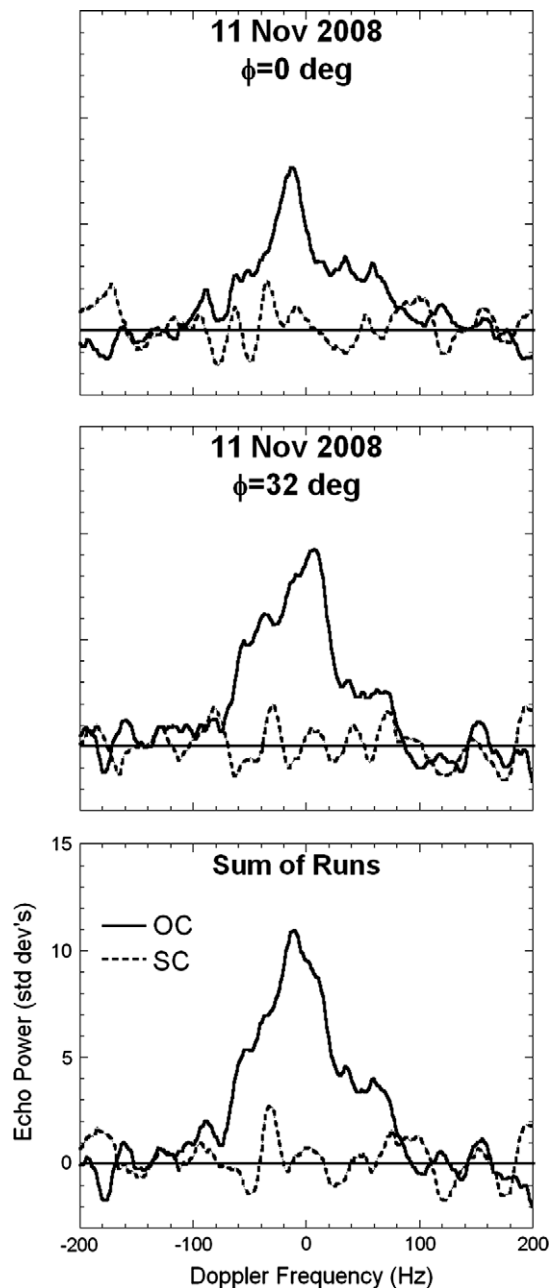


Fig. 4. CW observations of Hertha on 11 November 2008. The bottom panel shows the weighted sum of both runs. All runs have been smoothed to an effective frequency resolution of 20 Hz.

this is the interface involved in the echo (McKay et al., 1989). There is no significant region that is regolith-free. Both of these assumptions have been reinforced by spacecraft observations of both NEAs and MBAs (Sullivan et al., 2002; Farquhar et al., 2002) and theoretical studies on the fate of impact ejecta (Scheeres et al., 2002).

An important assumption of our analysis is that the regolith is *homogeneously* mixed, at least within the upper few meters of depth important for radar scattering and absorption. If metal particles within the regolith are of a significantly different size than the silicate particles, impact-induced shaking may give rise to a “brazil nut effect” (Rosato et al., 1987; Hong et al., 2001) so that the larger particles rise to the surface preferentially. In this event, the surface regolith may appear more silica- or metal-rich – depending upon which particles are larger – than the overall bulk composition. We assume that the bulk density of the upper meter

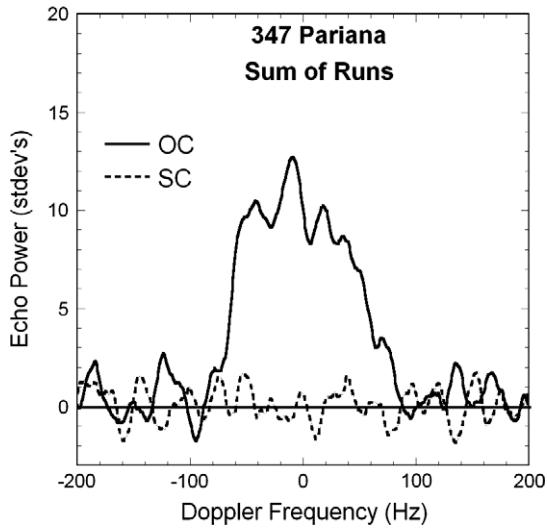


Fig. 5. Weighted sum of all runs for Pariana, smoothed to an effective frequency resolution of 15 Hz.

or so of the regolith is the physical property of an asteroid with the greatest effect on its radar echo. Metals have a higher conductivity than silicates and in solid form have nearly perfect radar reflectivity. However in powdered form – and especially when mixed with some silicates – their reflectivity is primarily a function of their bulk density (Ostro et al., 1985). With little data on the bulk porosity of asteroid regolith, we assume behavior similar to that measured on the lunar regolith. Numerous measurements and samples of the upper few meters of the lunar regolith were undertaken by Apollo astronauts and Soviet rovers. Although the upper few millimeters of the regolith have high porosity, as is evident from the strong optical opposition surge (Hapke, 1981), the upper meter or so is generally well packed, presumably from shaking due to impact generated shock waves (Carrier et al., 1991). Estimates of the porosity in the upper few centimeters are consistently around 50% and drop to values as low as ~40% within 60 cm of the surface (Carrier et al., 1991). The “best estimate” of *in situ* porosity (intra- and inter-granular) for the upper 60 cm of the lunar regolith is 46% (Carrier et al., 1991, Table 9.5), and we adopt 40–50% as an expected range.

We note that the near-surface bulk density is only that of the upper few meters of regolith and has little relationship to the bulk density of the asteroid as a whole. This latter property is dominated by gravitational collapse of pore space, whether the asteroid has been shattered and re-accreted as a “rubble pile”, and other considerations (Britt et al., 2002).

2.1.2. Model derivation

There have been a number of attempts to model radar reflectivity given the bulk density of an analog regolith. Both Ostro et al. (1985) and Garvin et al. (1985) provide empirical relationships between the density of powders and radar reflectivity as measured in the laboratory. Magri et al. (2001) develop twin models, one based on the Garvin et al. empirical model with additional theoretical considerations, and one based on the radar behavior of 433 Eros calibrated against spacecraft “ground-truth” obtained from the NEAR-Shoemaker mission to Eros. In this paper, we take elements from all three studies.

The Ostro et al. relationship is linear and given by

$$R = 0.12\rho - 0.13, \quad (5)$$

where R is the Fresnel radar reflectivity and ρ is the density of the sample (g cm^{-3}). Garvin et al. give a non-linear relationship which can be written (Magri et al., 2001)

$$R = \tanh^2\left(\frac{\rho}{6.4 \text{ g cm}^{-3}}\right). \quad (6)$$

Among the unknowns for applying these formulae to asteroids are: (a) the precise relationship between the radar albedo and Fresnel reflectivity (which is affected by the overall shape of the asteroid), and (b) the effects of surface roughness and volume scattering that give rise to the unexpected (SC) sense of the echo. The latter effect is probably of secondary importance for most of our targets because the polarization ratio of most main-belt asteroids is small. We therefore ignore it, and acknowledge that it may give rise to systematic errors that will affect our model results in roughly the same sense if not magnitude.

The relationship between radar albedo and Fresnel reflectivity is usually given as

$$\hat{\sigma}_{\text{OC}} = gR, \quad (7)$$

where g is a ‘gain factor’ that takes into account the non-spherical shape and surface irregularities of a real asteroid (Ostro et al., 1985). Following Magri et al. (2001), we assume $g = 1.2$ for our targets, indicating that our model targets return more energy than a perfect sphere.

There are two other data points which we can use to “calibrate” our model. Conservation of energy requires that a surface of $\rho = 0.0$ (i.e. no interface) should have no echo. Likewise, the very definition of radar albedo includes normalization to a metal sphere of the same size at the same location. We therefore take $\rho = 7.8 \text{ g cm}^{-3}$ (the density of FeNi) as the density we expect for a radar albedo of $\hat{\sigma}_{\text{OC}} = 1.0$.

A plot of both the Ostro et al. and Garvin et al. models (Fig. 12) shows that the Ostro et al. model satisfies our upper bound, but gives negative values of radar albedo for densities $< 1 \text{ g cm}^{-3}$. The Garvin et al. model satisfies our lower bound, but not the upper. We therefore adopt both models, but in a piecewise fashion:

$$\begin{aligned} \hat{\sigma}_{\text{OC}} &= 1.2 \tanh^2\left(\frac{\rho}{6.4 \text{ g cm}^{-3}}\right) & \text{for } \rho \leq 1.57 \text{ g cm}^{-3}, \\ \hat{\sigma}_{\text{OC}} &= 0.144\rho - 0.156 & \text{for } \rho > 1.57 \text{ g cm}^{-3}, \end{aligned} \quad (8)$$

or

$$\begin{aligned} \rho &= 3.20 \text{ g cm}^{-3} \ln\left(\frac{1 + \sqrt{0.83 \hat{\sigma}_{\text{OC}}}}{1 - \sqrt{0.83 \hat{\sigma}_{\text{OC}}}}\right) & \text{for } \hat{\sigma}_{\text{OC}} \leq 0.07, \\ \rho &= 6.944\hat{\sigma}_{\text{OC}} + 1.083 & \text{for } \hat{\sigma}_{\text{OC}} > 0.07. \end{aligned}$$

Surfaces composed of powdered metal, when compacted, become more electrically conductive and therefore more radar reflective. This phenomenon should cause the radar reflectivity to behave non-linearly at higher metal abundances as porosity is decreased and electrical contacts between adjacent metal grains increase. Because we lack empirical data in this range, we expect our model to be most accurate for metal abundances of ~50% or less.

It is reasonable to ask what level of confidence we can place in this model. Magri et al. (2007) summarize the results of all radar observations of MBAs up through 2003. The mean radar albedos reported for the various classes are: M (0.26 ± 0.17), S (0.14 ± 0.04), C (0.13 ± 0.05), and BGFPTD (0.09 ± 0.05). Looking first at the S-class, Eq. (8) gives surface densities of $2.0 \pm 0.2 \text{ g cm}^{-3}$. This value can be achieved with a typical ordinary chondrite grain density of 3.6 g cm^{-3} (Britt and Consolmagno, 2003) and a near-surface porosity of $45 \pm 5\%$. The mean C-class radar albedo suggests surface densities of $1.6\text{--}2.2 \text{ g cm}^{-3}$, consistent with analog grain densities of 2.6 g cm^{-3} (CM)– 3.5 g cm^{-3} (CO/CV) and surface porosities of ~40% (Britt and Consolmagno, 2003). The darker classes (BGFPTD) have radar albedos suggesting surface densities of $1.2\text{--}2.0 \text{ g cm}^{-3}$ which are consistent with lower density meteorite analogs such as CI’s (grain density 2.2 g cm^{-3} , Britt and Consolmagno, 2003) and Tagish Lake (overall density 1.7 g cm^{-3} , Hutchinson, 2004),

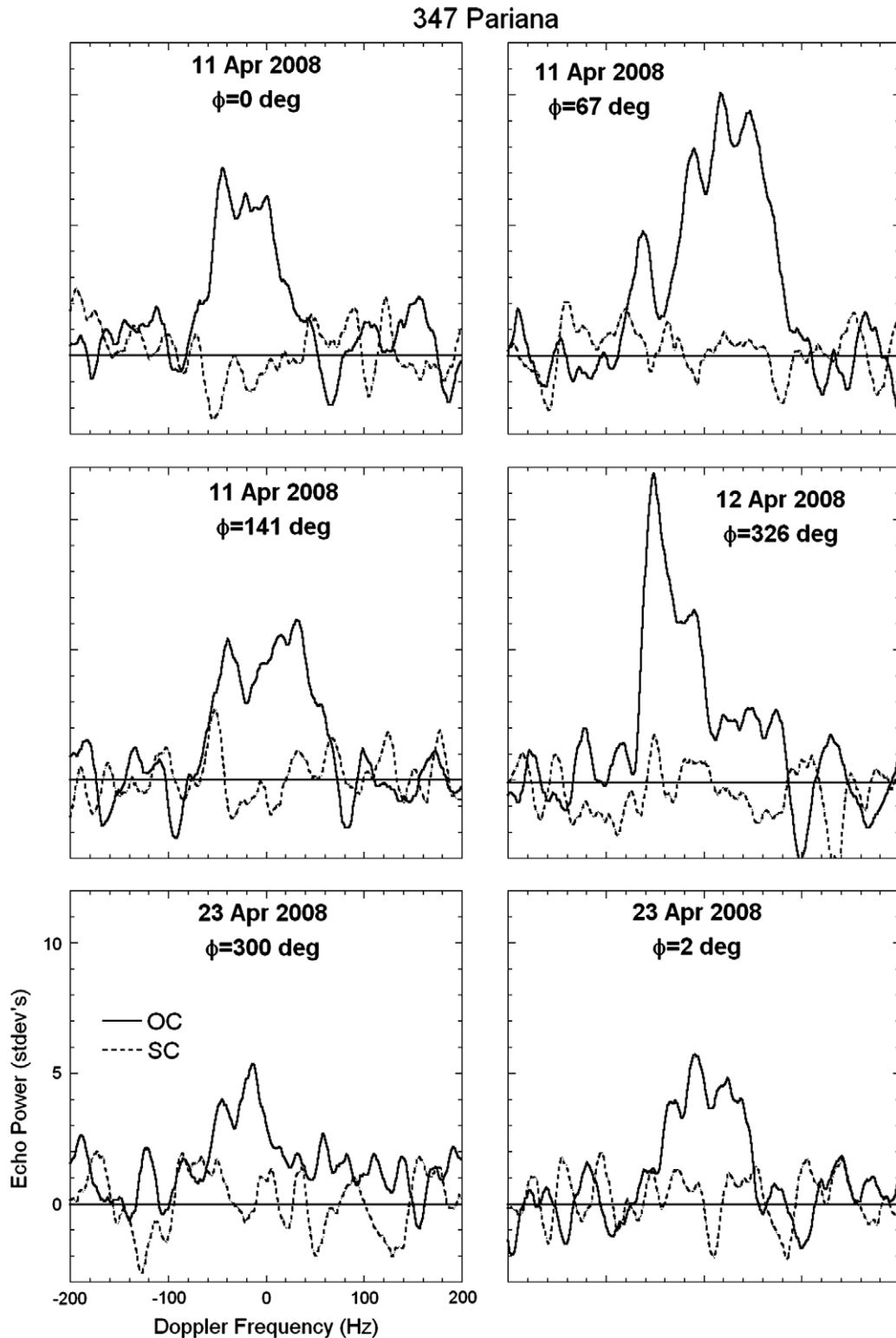


Fig. 6. Individual runs for Pariana, smoothed to an effective frequency resolution of 20 Hz and labeled with the rotation phase (ϕ , arbitrarily set to 0 for the first run).

greater surface porosity, or both. The higher M-class mean radar albedo suggests a significantly higher surface density than any other class and we postpone the discussion of it to a later section.

The results of the above analysis suggest that our simple model returns believable surface densities for the major asteroid classes given what we know of meteorite densities and believe we know about the regolith of the main-belt asteroids. In the next section,

we briefly review the characteristics of the meteorite analogs thought to make up the M-class asteroids.

2.2. Meteorite analogs of the M-class asteroids

Here we briefly examine the meteorite classes considered to be analogs for the M-class asteroids. We define the constraints

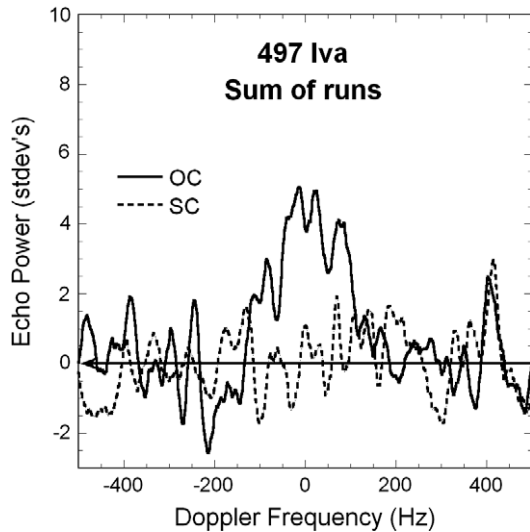


Fig. 7. Weighted sum of five runs of Iva, smoothed to an effective frequency resolution of 30 Hz.

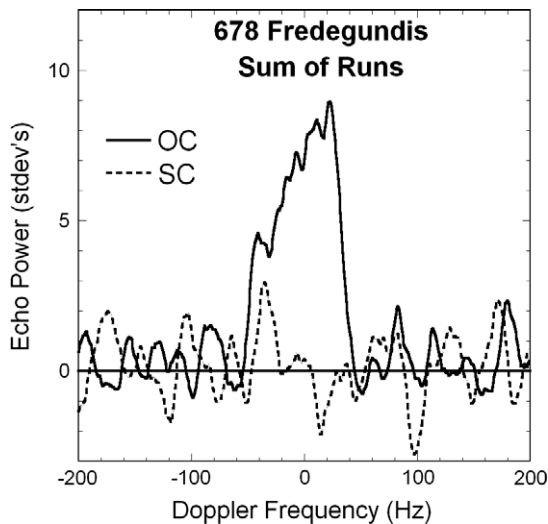


Fig. 8. Weighted sum of all runs of Fredegundis, smoothed to an effective frequency resolution of 15 Hz.

implied by each analog and discuss our ability to distinguish between them with radar as a proxy for bulk density. Properties of these analogs and our model-estimated radar albedos for them are summarized in Table 3.

2.2.1. Irons (FE)

Iron meteorites represent the canonical interpretation of the M-class as a remnant iron–nickel core of a shattered planetesimal (Gaffey and McCord, 1979; Bell et al., 1989). An iron interpretation suggests a very high temperature of formation. The cooling histories of iron meteorite parent bodies suggest that plausible diameters for exposed cores in the main-belt are 30–90 km (Haack et al., 1990; Rivkin et al., 2000). Given that these are thought to be remnant cores, there may or may not be some silicate from the mantle remaining (we assume no more than 10% of the asteroid) so that weak silicate absorption features (0.9 μm and 1.9 μm) are possible. We do not expect any spectroscopic features of hydration (e.g. 0.7 μm or 3 μm absorptions) due to the high temperature of formation. We assume grain densities of 7.5–7.8 g cm^{-3} .

2.2.2. Enstatite chondrites (EC)

Enstatite chondrites (EC) are primitive meteorites (i.e., they have not been substantially altered since formation) and formed in a highly reducing environment so that iron was not bound in the silicate fraction. Pure enstatite (an iron-free pyroxene) has no absorption features and when mixed with Fe/Ni-metal is difficult to spectroscopically distinguish from pure Fe/Ni-metal (Gaffey, 1976; Clark et al., 2004). The two varieties of EC are EH (high iron) and EL (low iron) that are distinguished primarily by metal abundance; this ranges from ~15% to 35% by volume (Britt and Consolmagno, 2003).

With a limited sample of EC meteorites for analysis, Britt and Consolmagno (2003) report grain densities of $\sim 3.6 \text{ g cm}^{-3}$. Given the known range of metal abundances and using endmembers of Fe/Ni-metal (7.8 g cm^{-3}) and enstatite (3.2 g cm^{-3}), we assume grain densities of 3.5–4.8 g cm^{-3} to be plausible. Although meteorite samples are anhydrous, Rivkin et al. (2000) suggest several hypothetical methods for aqueous alteration in the enstatite chondrite parent bodies.

2.2.3. High metal carbonaceous chondrites (CH/CB)

Subgroups of the larger CR meteorite clan (Krot et al., 2002), the unusual CH and CB carbonaceous chondrites have high concentrations of Fe/Ni-metal. CH (high metal) meteorites are polymict regolith breccias (Hutchinson, 2004) and have on the order of ~20% Fe/Ni-metal by volume, while the CB (Bencubbin-like) group can contain 40–75% Fe/Ni-metal (Krot et al., 2002). Hydrated minerals are sometimes found in the matrix of these meteorites (Greshake et al., 2002), so spectroscopic features consistent with hydrated minerals are possible. They are usually interpreted to be primitive meteorites because their refractory lithophile/Mg abundance ratios are similar to those of CI meteorites and because they show no evidence of thermal or shock metamorphism (Krot et al., 2002). However, some have argued that the CBs resulted from a protoplanetary impact between metal-rich and reduced-silicate objects (Campbell et al., 2002).

Assuming CH to have 15–25% Fe/Ni-metal and CB to have 40–75% Fe/Ni-metal, we get the following grain density estimates: CH 3.7–4.2 g cm^{-3} and CB 5.0–6.7 g cm^{-3} . Allowing for variations in porosity, these two meteorite classes essentially form a continuum of bulk density (Table 3). From a bulk density and radar perspective, an object composed of CH will be impossible to separate from one of EC, and a similar ambiguity exists for CB's and irons (see Table 3).

To our knowledge, only one CH sample (PCA 91467) has been spectroscopically measured in the laboratory; its visible/near-infrared spectrum looks like that of a “typical” carbonaceous chondrite with a gently sloped red continuum, shallow absorption feature at 0.9 μm , and a rounded visible region with a strong UV drop-off, and not at all like an iron-meteorite spectrum (steeply sloping red continuum, very weak UV drop-off) (Clark et al., 2009). It is also distinct from EC spectra, so while the radar data are ambiguous, it may be that the possible analogs (CH vs. EC) can be distinguished spectroscopically (Ockert-Bell et al., 2010). No CB spectra have been measured.

2.2.4. Carbonaceous chondrites (CI/CM)

Vilas (1994) suggested that some M-class asteroids may be primitive hydrous carbonaceous chondrites (CI and CM) which have been aqueously altered to a high degree. Rivkin et al. (2000) also discuss this as a possible scenario for the M-asteroids that have a 3 μm absorption feature (their W-class) but lack a 0.7 μm oxidized iron feature. The grain densities of the CI and CM meteorites are $\sim 2.5 \text{ g cm}^{-3}$, which is low compared with other chondrites (Britt and Consolmagno, 2003), and very low compared with irons.

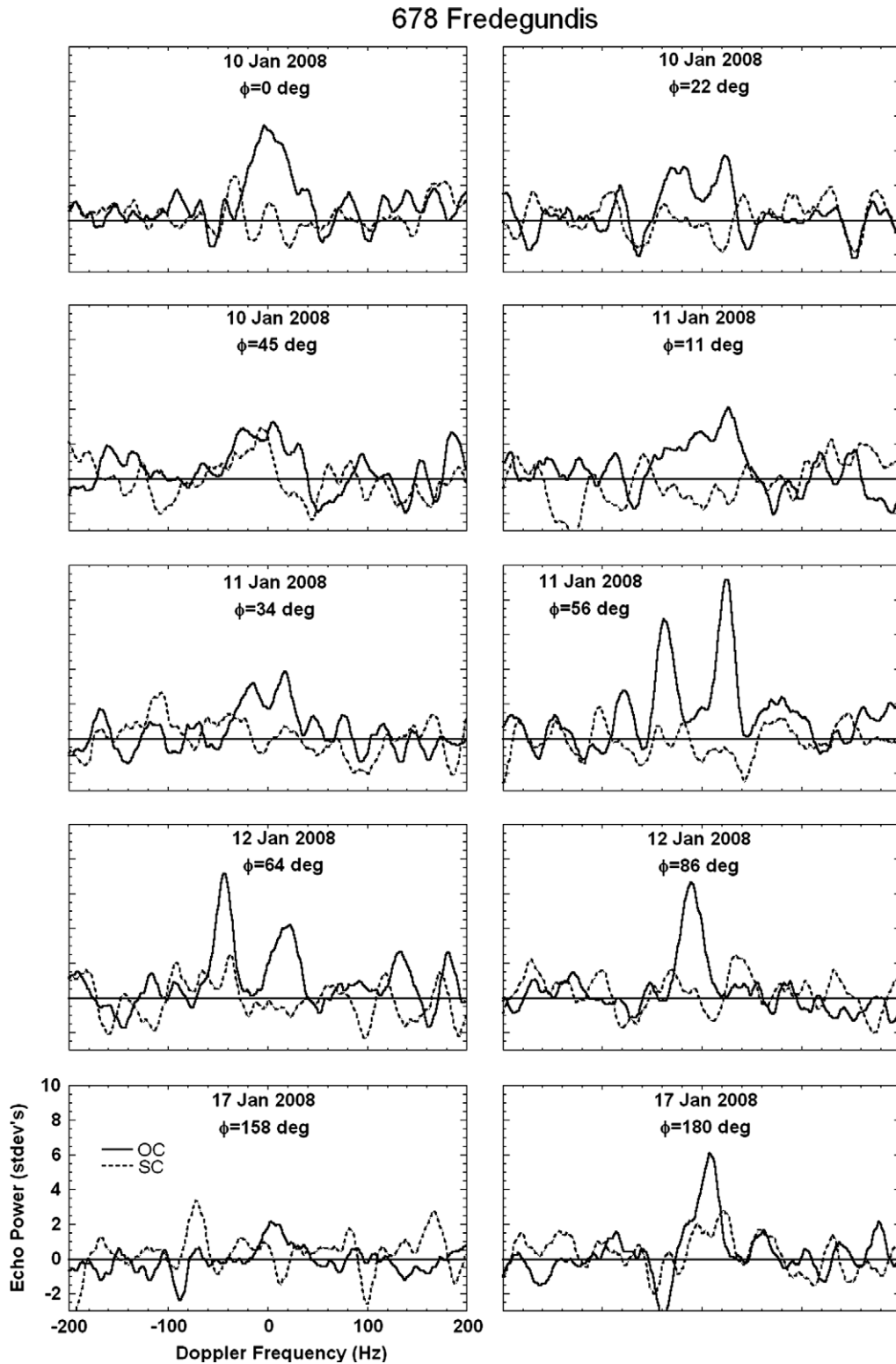


Fig. 9. Individual CW runs of 678 Fredegundis, smoothed to 20 Hz in frequency and labeled with the rotation phase (ϕ , arbitrarily set to 0 for the first run).

2.2.5. Stony-irons (SI)

Stony-irons are a large category of meteorites that include mesosiderites, pallasites, and numerous unique samples. All are characterized by subequal amounts of silicate and metal (Hutchinson, 2004). We use this category to refer to those analogs that are dominated by irons and silicates independent of any particular genesis.

Mesosiderites are brecciated mixtures of metal and silicates. The metal fraction appears to be genetically related to the IIIAB irons, while the silicate fraction is composed of fragments of igneous rocks, dominated by orthopyroxenes and Ca-rich plagioclase that appear similar to the Howardite–Eucrite–Diogenite (HED) assemblages found in basaltic achondrites (Hutchinson, 2004). There are no hydrated minerals of significance. There is no consensus

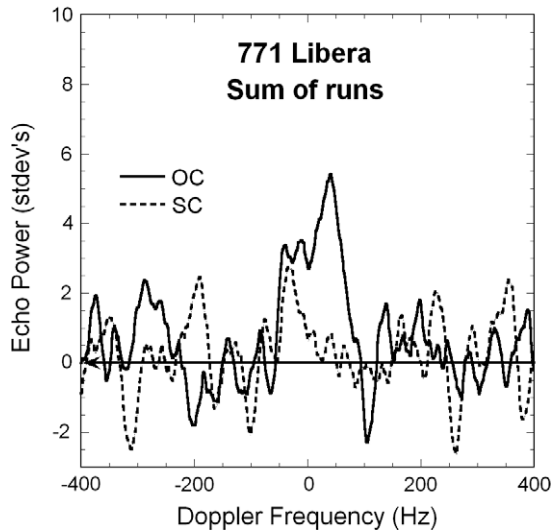


Fig. 10. Weighted sum of seven runs of 771 Libera, smoothed to an effective frequency resolution of 25 Hz.

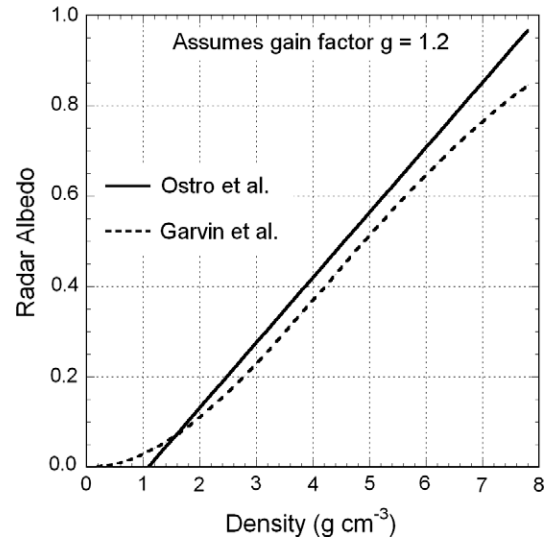


Fig. 12. Radar albedo versus bulk density for two models. Our model is a composite of the two and, for a given density, is equal to the higher radar albedo of the two models.

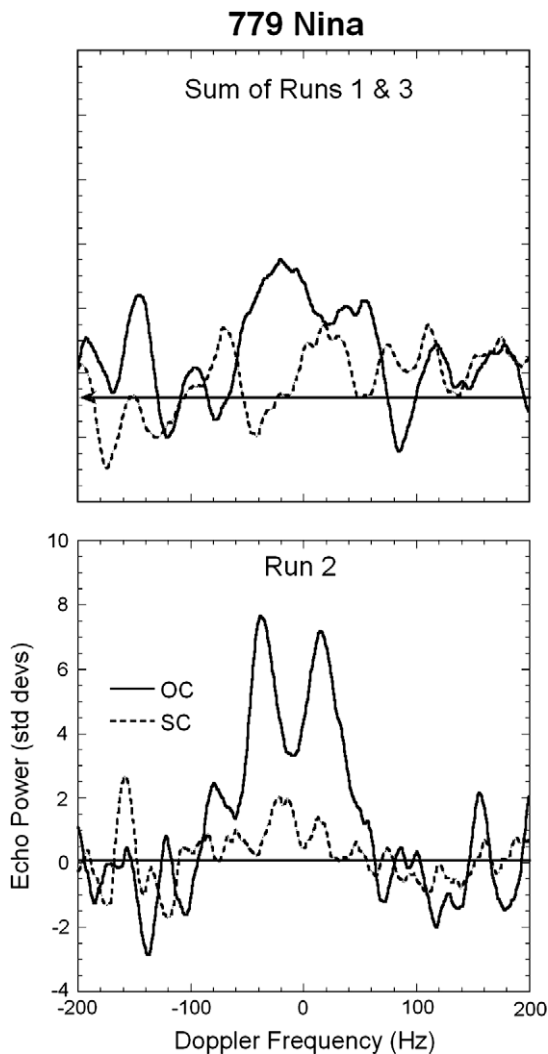


Fig. 11. CW spectra of Nina. Top is sum of runs 1 and 3 (rotation phase $\sim 0^\circ$), smoothed to an effective frequency resolution of 30 Hz; the bottom panel is run 2 (rotation phase $\sim 90^\circ$), smoothed to an effective frequency resolution of 20 Hz.

Table 3

Relationship between bulk density and radar albedo.

Type	% Vol. metal	ρ_{grain} (g cm^{-3})	ρ_{bulk} (g cm^{-3})	Radar albedo
FE	90+	7.5–7.8	3.8–4.7	0.39–0.53
EH/EL	15–35	3.5–4.8	1.8–2.9	0.10–0.26
SI	15–50	3.5–5.0	1.8–3.0	0.10–0.28
CH	15–25	3.5–4.2	1.8–2.5	0.10–0.20
CB	40–75	5.0–6.7	2.5–4.0	0.20–0.42
CI/CM	5<	2.3–2.6	1.2–1.6	0.04–0.08

Type indicates the meteorite analog. FE are irons dominated by Fe/Ni; EH/EL are enstatite chondrites; SI are stony-irons; CH and CB refer to the metal-rich carbonaceous chondrites; CI/CM are carbonaceous chondrites. Average grain densities are either from calculation from percentage of individual components or from measurements of Britt and Consolmagno (2003). Bulk density indicates the expected near-surface bulk density given the range of grain densities and porosity of 40–50%. Radar albedo is estimated from Eq. (8).

on their origin except that it appears to be complex and involve collisional disruption and re-accumulation (Hutchinson, 2004).

Pallasites are composed chiefly of low-iron olivine and metal that appears to be related to the IIIAB magmatic irons. A small percentage have a few volume percent of low Ca pyroxenes and are referred to as “pyroxene pallasites.” The traditional interpretation is that these represent fragments of the core/mantle boundary of early planetesimals.

Based on the presence of 0.9 and 2.0 μm absorption features in their telescopic spectra and in irradiated samples of the mesosiderite Vaca Muerta, Vernazza et al. (2009) suggested mesosiderite as a possible analog for the M-class asteroids (Xk in Bus and Binzel (2002) system) 201 Penelope, 250 Bettina, and 337 Devosa, and noted similarities in these spectra with those of 16 Psyche, 69 Hesperia, 110 Lydia, 125 Liberatrix, and 216 Kleopatra. Davis et al. (1998) suggested that 16 Psyche is a shattered and re-accreted differentiated parent body with irons and silicates remixed on the surface and the source of many mesosiderites.

The metal content of mesosiderites and pallasites range from 15% to $\sim 50\%$, Hutchinson (2004) and Britt and Consolmagno (2003) report grain densities of 4.4–4.8 g cm^{-3} for 20 pieces of nine different stony-iron meteorites. Using this information, we estimate grain densities of 3.5–5.0 g cm^{-3} to be plausible – essentially identical to the EH/EL analogs.

2.3. Analysis and discussion

Nineteen M-class MBAs have now been observed with radar. (We exclude 71 Niobe from Shepard et al. (2008a) because newer spectral evidence (Ockert-Bell et al., 2010) indicates it is L-class.) In this section, we summarize what we have learned from our observations of these 19 objects. Table 4 and Fig. 13 summarize the basic physical and radar properties of each target.

2.3.1. Collisional history

Many of our objects show evidence for a significant collisional history, including irregular shapes, global-scale concavities, or bifurcation. 16 Psyche has aspects where only one lightcurve maximum/minimum is observed and coarse radar images show irregularity (cf. Shepard et al., 2008a and references therein). 22 Kalliope was the first known M-class binary (Margot and Brown, 2003; Descamps et al., 2008). 216 Kleopatra is a known twin-lobed structure (Ostro et al., 2000; Tanga et al., 2001) and was recently discovered to have two satellites (Marchis et al., 2008). 678 Fredegundis shows strong evidence of bifurcation and a lightcurve consistent with a compact contact binary or bi-lobed structure (Stephens et al., 2008). 110 Lydia, 129 Antigone, 758 Mancunia, and 779 Nina also show evidence of bifurcation or global-scale concavities at some rotation phases (Shepard et al., 2008a and this paper). The proportion of objects in our sample with large-scale features like these is probably an underestimate because the SNR for 224 Oceana, 325 Heidelberga (both described in Shepard et al. (2008a)), 497 Iva, and 771 Libera did not allow for rotationally resolved analysis. In all, at least 10% of our objects are multiple systems, and another 30% show evidence for major collisional events.

2.3.2. Composition

2.3.2.1. General trends and interpretations. The high to very high radar albedo of all the M-class asteroids examined, excepting only 83 Beatrix, suggests their surface bulk density is significantly higher than the non-M-class asteroids. Using the model described by Eq. (8), we estimate the near-surface bulk density of the mean M-class asteroid to be $3.0 \pm 0.9 \text{ g cm}^{-3}$, or about 50% higher than the average S-class surface density ($2.0 \pm 0.2 \text{ g cm}^{-3}$) computed earlier. A

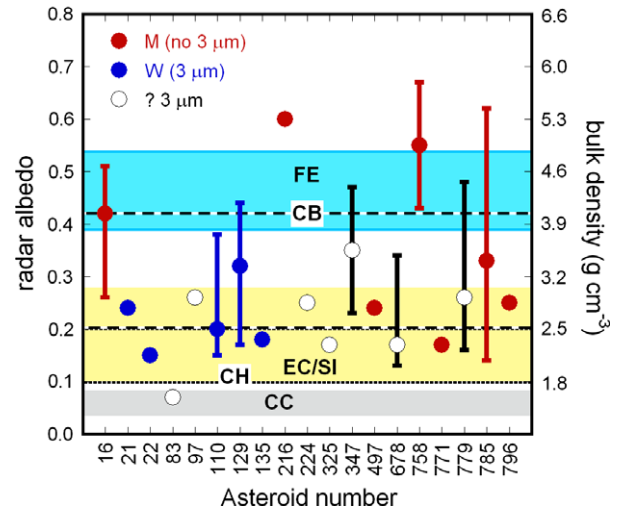


Fig. 13. Radar albedo for every main-belt M-class target observed by radar. Right y-axis shows the near-surface bulk density estimated from our model (Eq. (8)). Colored regions show range of radar albedos expected for compositional analogs described in the text and Table 3: gray is carbonaceous chondritic (CC), yellow is enstatite chondritic (EC) and stony-irons (SI), and blue is dominantly metallic (FE). Dashed lines show the range expected for CH (short dashes) and CB (long dashes). Red solid circles are M-class objects with no observed 3 μm feature. Blue circles are Rivkin et al. (2000) W-class objects (M-class with a 3 μm feature). Open circles are M-class objects that have not been observed in the 3 μm region. The uncertainties shown are for asteroids which exhibit significant variation with rotation phase – those error bars show the range of radar albedos observed. To determine whether an asteroid belongs to the Mm-class, we use the highest radar albedo indicated (top of uncertainty bar). Other uncertainties could potentially shift each target up or down by 25%, but these are not shown for clarity. (For interpretation of the references to color in this figure legend, the reader is referred to the web version of this article.)

density this large in a regolith of reasonable porosity requires a high concentration of dense phases like iron/nickel or possibly metal oxides or sulfides. It thus seems likely that few of the M-class MBAs are highly aqueous-altered carbonaceous chondrites (CI or CM) as proposed by Vilas (1994). Table 4 lists our best estimate of meteorite analogs for each asteroid.

Table 4
M- and X-class asteroids observed by radar.

Asteroid	D (km)	p_v	P (h)	σ_{OC}	μ_c	Analog	Tholen	Bus–DeMeo	Rivkin	This paper
16 Psyche	186 ± 30	0.23 ± 0.05	4.196	0.42 ± 0.10	0.06 ± 0.02	FE, CB	M	Xk	M	Mm
21 Lutetia	100 ± 11	0.20 ± 0.03	8.172	0.24 ± 0.07	0.22 ± 0.05	EC, CH	M	Xc	W	
22 Kalliope	162 ± 3	0.14 ± 0.01	4.148	0.18 ± 0.05	0.07 ± 0.10	CH, EC	M	Xk	W	
83 Beatrix	81 ± 2	0.09 ± 0.01	10.16	0.07 ± 0.03	0.23 ± 0.11	CC	X	X		
97 Klotho	83 ± 5	0.23 ± 0.03	35.15	0.26 ± 0.05	0.24 ± 0.02	EC, CH	M	Xc		
110 Lydia	89 ± 9	0.16 ± 0.02	10.926	0.20 ± 0.12	0.02 ± 0.02	CB, CH	X	Xk	W	
129 Antigone	113 ± 12	0.21 ± 0.05	4.957	0.36 ± 0.09	0.14 ± 0.02	CB?	M	Xk	W	Mm
135 Hertha	77 ± 7	0.14 ± 0.01	8.401	0.18 ± 0.05	0.10 ± 0.03	CH, EC	M	Xk	W	
216 Kleopatra	124 ± 15	0.12 ± 0.02	5.385	0.60 ± 0.15	0.00 ± 0.04	FE	M	X	M	Mm
224 Oceana	62 ± 2	0.17 ± 0.01	9.388	0.25 ± 0.10	0.33 ± 0.06	EC, CH	M	Xc		
325 Heidelberga	76 ± 2	0.11 ± 0.01	6.737	0.17 ± 0.08	0.0 ± 0.1	SI, EC	M	-		
347 Pariana	51 ± 5	0.18 ± 0.02	4.053	0.36 ± 0.09	0.05 ± 0.03	FE, CB	M	Xk		Mm
497 Iva	40 ± 8	0.13 ± 0.03	4.62	0.24 ± 0.08	0.11 ± 0.03	SI, CH	M	Xk	M	
678 Fredegundis	42 ± 4	0.25 ± 0.02	11.62	0.18 ± 0.05	0.03 ± 0.06	SI, CB	X	Xk		
758 Mancunia	85 ± 7	0.13 ± 0.02	12.738	0.55 ± 0.14	0.34 ± 0.03	FE, CB	X	Xk	M	Mm
771 Libera	29 ± 2	0.13 ± 0.01	5.892	0.17 ± 0.04	0.37 ± 0.09	SI, CH	X	Xk	M	
779 Nina	77 ± 2	0.14 ± 0.01	11.186	0.26 ± 0.24	0.17 ± 0.07	FE, CB	X	Xk		Mm
785 Zwetana	49 ± 2	0.12 ± 0.01	8.919	0.33 ± 0.08	0.17 ± 0.03	FE, CB	M	Cb	M	Mm
796 Sarita	45 ± 2	0.20 ± 0.01	7.75	0.25 ± 0.10	No data	SI	XD	S	M	

Notes: D is asteroid effective diameter, p_v is visual albedo, P is rotation period, σ_{OC} is radar albedo, Analog suggests the one or two most likely meteorite analogs given the observed radar albedo and the estimated near-surface bulk density (FE = iron–nickel, EC = enstatite chondrite (EH or EL), CH and CB = high-iron carbonaceous chondrites, CC = hydrated carbonaceous chondrites, SI = stony-irons. See text for details), and μ_c is circular polarization ratio. The classifications listed are based on the following references: Tholen (1984), Bus and Binzel (2002), DeMeo et al. (2009), and Rivkin et al. (2000). This paper (this work). Uncertainties are listed for all quantities except the rotation period, which is on the order of the last significant digit. Diameters and visual albedos are primarily from the IRAS data set (Tedesco et al., 2002) except where modified by others or our previous radar data (see text and Shepard et al., 2008a and references therein).

Seven asteroids have radar albedos, at some or all rotation phases that are easily consistent with the interpretation that these objects are dominated by iron–nickel: 16 Psyche, 129 Antigone, 216 Kleopatra, 347 Pariana, 758 Mancunia, 779 Nina, and 785 Zwetana. The mean radar albedo for these objects is $\hat{\sigma}_{oc} = 0.41 \pm 0.13$, approximately three times higher than the average S-class asteroid (Magri et al., 2007). Eq. (8) suggests a mean surface density of 4.0 g cm^{-3} , consistent with NiFe metal and $\sim 50\%$ porosity. Given this well separated group of M-class asteroids which fit the very high metal interpretation, we propose to use the designation Mm (M-class, very high metal abundance) for these to separate them from the other M-class objects. Note that, of this group, only 129 Antigone has a $3 \mu\text{m}$ feature (Table 4). These objects (one-third of our sample) are the candidates most likely to be collisionally exposed cores or core fragments. However, other information (diameter, shape, and spectroscopic absorption features) must be included before making this determination. We discuss this in the following section for individual objects.

Two asteroids, 110 Lydia and 678 Fredegundis, have radar albedos at some rotation phases that suggest a moderately high metal content. Lydia has a $3 \mu\text{m}$ absorption feature while Fredegundis has not been observed at $3 \mu\text{m}$. Given their more modest radar albedos and evidence of hydration for Lydia, neither of these is likely to be a remnant metal core.

The remaining 10 asteroids have a higher mean radar albedo ($\hat{\sigma}_{oc} = 0.20 \pm 0.06$) than any other class, but are not high enough to be metallic cores. Approximately half of these have a $3 \mu\text{m}$ feature in their spectra. If we ignore the Mm asteroids and plot radar albedo versus visual albedo for these 10 objects plus Lydia and Fredegundis, a positive linear correlation becomes evident (Fig. 14). If we exclude 83 Beatrix as a possible outlier, the correlation is still evident and significant but has a shallower slope. Powdered metals in laboratory measurements tend to have visual albedos ~ 0.10 – 0.15 (Cloutis et al., 2009). So while it is tempting to postulate that metal content drives both the optical and radar albedos, the laboratory data do not seem to support this. Perhaps there is an accessory feature associated with higher metal content that is responsible for the apparent correlation.

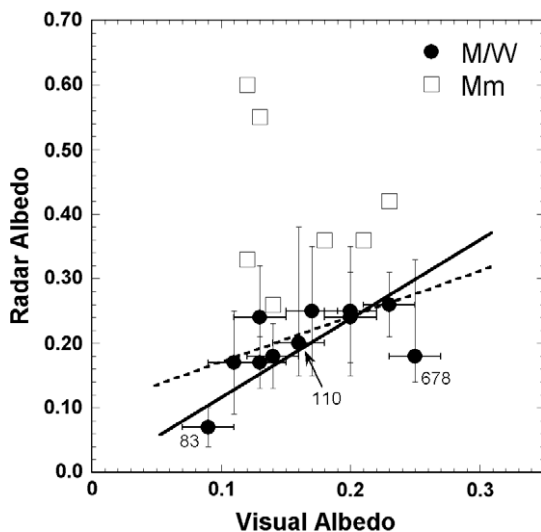


Fig. 14. Plot of radar albedo versus visual albedo for all M asteroids observed by radar. The line shows the best linear fit to all these targets excluding the Mm's (squares). Radar albedo uncertainties for 110 and 678 are asymmetric; we used the average of their range as their respective standard deviations in the formal fit. The best fit line is $\hat{\sigma}_{oc} = (-0.01 \pm 0.05) + (1.25 \pm 0.35)p_v$ with a correlation coefficient of 0.86. The best fit line for the data excluding 83 Beatrix (dashed) is $\hat{\sigma}_{oc} = (0.10 \pm 0.08) + (0.64 \pm 0.46)p_v$ with a correlation coefficient of 0.73.

Eleven of our targets, including most of our high albedo (Mm) objects, are classified as Xk in the Bus–DeMeo system (Table 4). These objects have VISIR spectra with significant red-slopes and $0.9 \mu\text{m}$ and $1.9 \mu\text{m}$ absorption features, consistent with the presence of silicates on their surfaces. Of these 11 objects, four show a $3 \mu\text{m}$ feature, four show no evidence of such a feature, and three have not been observed at that wavelength. Lupishko and Belskaya (1989) were perhaps the first to suggest that most M-class asteroids have a significant silicate component based on optical polarimetry of M-asteroids and laboratory samples. Vernazza et al. (2009) show that Xk spectra are very similar to laboratory spectra of mesosiderites and suggest this interpretation for several Tholen M and Bus Xk asteroids. They note, as have others, that the presence of significant metal severely mutes the silicate absorption features of their laboratory VISIR spectra.

Given these observations, along with models and evidence that indicate most of the main-belt asteroids are collisionally evolved, i.e. shattered or disrupted and re-assembled (Asphaug et al., 2002; Richardson et al., 2002), we propose that most of the M-class asteroids resulted from collisions between iron (core or core fragment) and silicate bodies and their disruption and eventual re-accretion. The relative sizes and compositions of the colliding objects determine whether the final composition is dominated by metal or silicates. This interpretation suggests that composite and brecciated compositions like the stony-irons and high-iron carbonaceous chondrites are the norm for M-class objects. The roughly equal split between those with a $3 \mu\text{m}$ feature and those without is consistent with the stochastic nature of this model. And while we have assumed upper bounds on the iron content of these objects based on a limited set of stony-iron meteorite samples, we see no reason why there should not be a continuum of metal abundance ranging from a lower bound of $\sim 25\%$ up to 100% in the general M-population.

2.3.2.2. Best analogs for individual targets. Asteroid 16 Psyche is the largest M-class asteroid known. Early estimates put the diameter at about 250 km (Tedesco et al., 2002), but more recent polarimetric (Lupishko, 2006) and radar estimates (Shepard et al., 2008a) place it closer to 200 km. In any event, Psyche is still far larger than the 30–90 km diameter expected for a remnant core (Haack et al., 1990; Rivkin et al., 2000). Its shape is irregular (Shepard et al., 2008a and references therein), its radar albedo is less than that of Kleopatra, Zwetana, or Mancunia, and the presence of a $0.9 \mu\text{m}$ absorption feature and Xk classification suggests a significant silicate component. All of these lead us to speculate that Psyche is a collisional aggregate of one or more objects, at least one of which had a significant metal content. The interpretation of Davis et al. (1998) – that Psyche resulted from the complete disruption and reassembly of a differentiated parent body – is favored less because a significant fraction of total free metal must eventually be segregated into the upper regolith (assuming Psyche began with a chondritic composition). If Psyche is of mesosiderite composition, as suggested by Davis et al. (1998), then our radar model suggests its regolith is dominated by metal instead of silicate.

Birlan et al. (2006) and Barucci et al. (2008) have suggested carbonaceous chondrites, in particular CO and CV, as good analogs for 21 Lutetia. The difficulty with this interpretation is that the estimated bulk density of a CO/CV surface is $\sim 2.0 \text{ g cm}^{-3}$ based on published grain densities (Britt and Consolmagno, 2003). Lutetia's radar albedo (0.24) and our model suggest a surface bulk density closer to 2.8 g cm^{-3} , or 40% higher than expected for these materials. Lazzarin et al. (2009) suggested CH/CB meteorites as analogs for Lutetia; these might satisfy both the spectral and radar data, but as noted earlier, spectral data for the CH/CB meteorites are rare. Alternatively, Vernazza et al. (2009) hypothesized that both Lutetia and 97 Klotho are composed of enstatite chondrites based

on their spectral similarity to laboratory spectra of the EL6 Eagle meteorite. Both asteroids lack obvious spectral absorption features and have similar optical (0.20 and 0.23) and radar albedos (0.24 and 0.25). To this we add that both objects are Xc in the Bus–DeMeo (DeMeo et al., 2009) classification scheme (Ockert-Bell et al., 2010). In our sample, 224 Oceana also lacks spectral absorption features, is classified as an Xc, and has similar optical and radar albedos (0.17 and 0.25, respectively) to those of Lutetia and Klotho. We therefore suggest that these three objects are of similar composition and are probably composed of either EC or CH. The July 2010 fly-by of Lutetia by the Rosetta spacecraft may help resolve this issue.

Asteroid 83 Beatrix is an X-class object in both the Tholen and Bus classification schemes, and its optical albedo (0.09 ± 0.01) is at the lower boundary of the M-class range. Based on its low radar albedo, we suggest 83 Beatrix may be a carbonaceous chondrite and possibly an aqueously altered CI or CM as proposed by Vilas (1994). No 3 μm observations of Beatrix have been reported.

Asteroid 216 and sixteen Kleopatra was not observed as part of this study, but was observed by Mitchell et al. (1995) and Ostro et al. (2000). Its high radar albedo of 0.6 leaves little doubt that it is a metallic object. However, its ‘dog-bone’ or bi-lobate shape (Ostro et al., 2000; Tanga et al., 2001) and the existence of two moonlets (Marchis et al., 2008) are strong evidence for a significant collisional history. Is Kleopatra the unlikely result of a collision and fusion between two cores or core fragments? The ends of the ‘bone’ are both ~ 70 km in diameter, within the bounds expected for core remnants noted previously.

Asteroid 785 Zwetana has a strong red spectral slope and shows no spectral absorption features in the near-infrared. Its Cb classification (Bus and Binzel, 2002; DeMeo et al., 2009) is primarily based on a visible spectrum taken by Bus and Binzel (2002). Newer visible spectra by Fornasier et al. (2009) are unlike those previous and more consistent with the Tholen M-class. Zwetana shows extreme variations in radar albedo (0.10–0.60, Shepard et al., 2008a) and is also the smallest Mm-class object ($D_{\text{eff}} = 49$ km) in our sample. Given these characteristics, we suggest that Zwetana is the most likely member of our sample to be a pure remnant metal core or a fragment of such an object. We discuss its radar albedo variability in the next section.

Based on their sizes and high radar albedos, 347 Pariana, 758 Mancunia, and 779 Nina must also be considered as possible remnant cores. Their Xk classification is consistent with our assumption that remnant cores may retain a $\sim 10\%$ silicate fraction. However, only Mancunia is apparently anhydrous; no 3 μm data have been obtained for Pariana or Nina.

Asteroid 796 Sarita was originally classified as XD by Tholen (1984), but more recent spectral work (Ockert-Bell et al., 2010) indicates it to be an S-class. Rivkin et al. (2000) detect no 3 μm in its spectrum. Given its moderately high radar albedo (0.25, Magri et al., 1999), we suggest it to be a good candidate for a stony-iron (mesosiderite) instead of the more traditional ordinary chondrite interpretation.

2.3.3. Rotational variability

An intriguing result of this and our previous work (Shepard et al., 2008a) is that all of the higher radar albedo targets show large variations in radar albedo as they rotate. However, for those targets with rotationally resolved optical or thermal spectra as well, we see little or no evidence for compositional variation with rotation phase. With the exception of 216 Kleopatra (Ostro et al., 2000), none of these are highly elongated or have significant light-curve amplitudes. 785 Zwetana (Shepard et al., 2008a) is an extreme case and displays variations in radar albedo ranging from

a high of 0.6 to a low of 0.1. These variations were observed over two rotation cycles.

To explain variations in radar albedo with no accompanying spectral variations, Shepard et al. (2008a) suggested that regolith depth may vary, or regolith density may increase in such a way (in some places) to absorb the radar energy. Another possibility suggested specifically for Zwetana is that the surface is not metallic, but that two large facets on opposite sides are oriented to specularly backscatter the radar giving anomalously large echoes at those rotation phases. This was hypothesized because the radar albedo was observed to drop dramatically within a relatively short rotation interval of $\sim 40^\circ$. However, this latter explanation seems contrived and is not very satisfying.

Further consideration and the continually accumulating catalog of irregular asteroid shapes lead us to suggest a new explanation. If a metallic Zwetana had tapered ends (or any irregular shape that has most of the surface facets at that aspect NOT facing the Earth), it would appear darker to the radar when those ends were oriented toward Earth because most of the incident energy would reflect away from the Earth. This is similar to the design principle used in “stealth” aircraft. Further, as the asteroid rotated, the radar albedo would change rapidly around these regions depending upon the orientation of the surface facets. This may explain why all of the radar bright asteroids show significant radar albedo variations with rotation.

To illustrate with a simplified example, consider a silicate-rich asteroid with surface bulk density of 1.75 g cm^{-3} (grain density 3.5 g cm^{-3} and 50% porosity). Its reflection coefficient is $R = 0.08$ (taking the average from Eqs. (5) and (6)), meaning that 8% of the incident energy is reflected from every ‘surface facet’ in the general specular direction, and the remaining 92% is absorbed or scattered into multiple directions including the backscatter direction. However a asteroid dominated by metal with a surface bulk density of 3.75 g cm^{-3} (grain density 7.5 g cm^{-3} and 50% porosity) has a reflection coefficient of $R = 0.30$. Facets on this asteroid reflect four times more energy into the specular direction and have correspondingly less absorbed or scattered into multiple directions. On a metal-rich asteroid, the amount of power backscattered to the Earth is therefore more sensitive to surface irregularities than on a rocky asteroid and is likely to show more variability. An example supporting this interpretation is the small metallic near-Earth asteroid (6178) 1986 DA (Ostro et al., 1991). This object is about 2 km in diameter and has a modestly elongated convex hull (~ 1.4), but its OC radar cross-section varies by a factor of four with rotation.

2.3.4. No observed correlation of radar albedo with polarization ratio or size

Benner et al. (2008) and Shepard et al. (2008b) found that E- and V-class asteroids have the highest circular polarization ratios of any class, suggesting a compositional control on this radar parameter. A histogram of circular polarization ratio for the M-asteroids (Fig. 15) shows no trend. Polarization ratios show a decline in frequency from 0.0 to nearly 0.4, but this is more-or-less consistent with the behavior of the MBAs as a group (Magri et al., 2007). All but one of the Mm’s have polarization ratios $\mu_c \leq 0.17$, but with a sample size of only seven, it is not clear if this is significant or not.

Rivkin et al. (2000) found that asteroids with diameters larger than 65 km tend to show a 3 μm feature, while those smaller than 65 km tend not to show a 3 μm feature. Based on this finding, they hypothesized that the smaller objects were anhydrous cores and the larger objects were primitive materials such as enstatite or carbonaceous chondrites. Our results are not consistent with this hypothesis. The diameters of the apparently anhydrous Mm’s are 186 km, 124 km, 85 km, and 49 km.

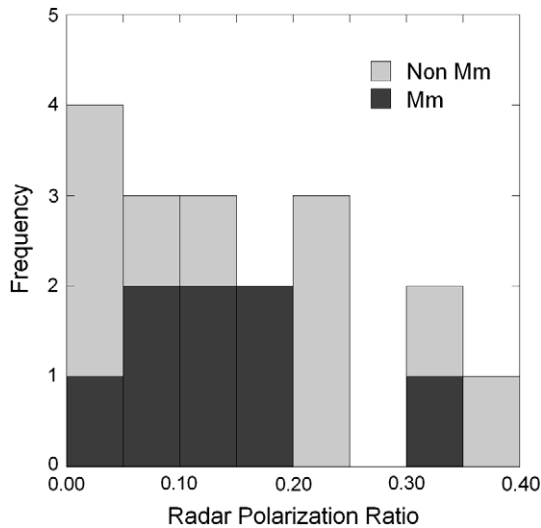


Fig. 15. Histogram of circular polarization ratio for all main-belt M-class asteroids for which this data is available (no circular polarization data is available for 796 Sarita).

2.4. Conclusions

The evidence of our radar-detected sample, combined with the spectral observations of others, leads us to conclude that few of the Tholen M-class asteroids are pristine remnant cores. Of our sample of 19 asteroids, only 785 Zwetana seems to fit in all categories of radar albedo, diameter, and spectral properties. Three other asteroids, 347 Pariana, 758 Mancunia, and 779 Nina may also be remnant cores with a modest residual silicate component. Based on its radar albedo and shape, 216 Kleopatra may be a collisional composite of core materials from two separate objects. Only three of our sample – 21 Lutetia, 97 Klotho, and 224 Oceana – have radar and VISIR spectral properties consistent with enstatite chondrites, but they may also be high metal carbonaceous chondrites (CH). The remaining objects have spectral features that indicate the presence of iron-poor silicates and, in about half of the cases, possible hydrated phases. We suggest that the majority of these objects are collisional composites of metallic and silicate objects with compositions more like stony-irons or high-iron carbonaceous chondrites. This interpretation is consistent with our evidence for significant collisional histories on these objects, and current models that suggest most of the main-belt asteroids have been either collisionally disrupted or shattered and re-accreted at some point in their history. Because of the limited delivery pathways for meteorites to reach the Earth, we may not have true samples of these objects in our collections.

Acknowledgments

We dedicate this paper to the memory of Steven J. Ostro – friend, colleague, and mentor. Reviews by P. Hardersen and L. Lim improved the manuscript. M.K.S. and B.E.C. gratefully acknowledge support from NSF Grants AST-0605903 and AST-0606704. A.W.H. and B.D.W. acknowledge support from NASA Grant NNG06G132G and NSF Grant AST-0607505. The Arecibo Observatory is part of the National Astronomy and Ionosphere Center, which is operated by Cornell University under a cooperative agreement with the National Science Foundation. We thank the technical staff at the observatory for help with observations. Some of this work was performed at the Jet Propulsion Laboratory, California Institute of Technology, under contract with the National Aeronautics and Space Administration. This material is based in

part upon work supported by the National Aeronautics and Space Administration (NASA) under the Science Mission Directorate Research and Analysis Programs.

References

- Asphaug, E., Ryan, E.V., Zuber, M.T., 2002. Asteroid interiors. In: Bottke, W.F., Jr., Cellino, A., Paolicchi, P., Binzel, R.P. (Eds.), *Asteroids III*. University of Arizona, Tucson, pp. 463–484.
- Barucci, M.A., and 10 colleagues, 2008. Asteroids 2867 Steins and 21 Lutetia: Surface composition from far infrared observations with the Spitzer space telescope. *Astron. Astrophys.* 477, 665–670.
- Bell, J.F., Davis, D.R., Hartmann, W.K., Gaffey, M.J., 1989. Asteroids: The big picture. In: Binzel, R.P., Gehrels, T., Matthews, M.S. (Eds.), *Asteroids II*. University of Arizona, Tucson, pp. 921–948.
- Belskaya, I.N., Lagerkvist, C.I., 1996. Physical properties of the M-class asteroids. *Planet. Space Sci.* 44, 783–794.
- Benner, L.A.M., and 10 colleagues, 2008. Near-Earth asteroid surface roughness depends on compositional class. *Icarus* 198, 294–304.
- Birlan, M., Vernazza, P., Fulchignoni, M., Barucci, M.A., Descamps, P., Binzel, R.P., Buz, S.J., 2006. Near infrared spectroscopy of the Asteroid 21 Lutetia. I. New results of long-term campaign. *Astron. Astrophys.* 454, 677–681.
- Birlan, M., Vernazza, P., Nedelcu, D.A., 2007. Spectral properties of nine M-type asteroids. *Astron. Astrophys.* 475, 747–754.
- Britt, D.T., Consolmagno, G.J., 2003. Stony meteorite porosities and densities: A review of data through 2001. *Meteorit. Planet. Sci.* 38, 1161–1180.
- Britt, D.T., Yeomans, D., Housen, K., Consolmagno, G., 2002. Asteroid density, porosity, and structure. In: Bottke, W.F., Jr., Cellino, A., Paolicchi, P., Binzel, R.P. (Eds.), *Asteroids III*. University of Arizona, Tucson, pp. 485–500.
- Bus, S.J., Binzel, R.P., 2002. Phase II of the Small Main-belt Asteroid Spectroscopic Survey: A feature-based taxonomy. *Icarus* 158, 146–177.
- Campbell, A.J., Humayn, M., Weisberg, M.K., 2002. Siderophile element constraints on the formation of metal in the metal-rich chondrites Bencubbin, Weatherford, and Gujba. *Geochim. Cosmochim. Acta* 66, 647–660.
- Carrier III, W.D., Olhoef, G.R., Mendell, W., 1991. Physical properties of the lunar surface. In: Heiken, G.W., Vaniman, D.T., French, B.M. (Eds.), *Lunar Sourcebook: A User's Guide to the Moon*. Cambridge University Press, NY, pp. 475–594.
- Cellino, A., Zappala, V., Doressoundiram, A., Di Martino, M., Bendjoya, Ph., Dotto, E., Migliorini, F., 2001. The puzzling case of the Nysa–Polana family. *Icarus* 152, 225–237.
- Cellino, A., Diolaiti, E., Ragazzoni, R., Hestroffer, D., Tanga, P., Ghedina, A., 2003. Speckle interferometry observations of asteroids at TNG. *Icarus* 162, 278–284.
- Chapman, C.R., Salisbury, J.W., 1973. Comparisons of meteorite and asteroid spectral reflectivities. *Icarus* 19, 507–522.
- Clark, B.E., Bus, S.J., Rivkin, A.S., Shepard, M., Shah, S., 2004. Spectroscopy of X-type asteroids. *Astron. J.* 128, 3070–3081.
- Clark, B.E., Ockert-Bell, M.E., Cloutis, E.A., Mothé-Diniz, T., Bus, S.J., 2009. Spectroscopy of K-complex asteroids: Parent bodies of carbonaceous meteorites? *Icarus* 202, 119–133.
- Cloutis, E.A., Gaffey, M.J., Smith, D.G.W., Lambert, R.St.J., 1990. Metal silicate mixtures: Spectral properties and applications to asteroid taxonomy. *J. Geophys. Res.* 95, 8323–8338.
- Cloutis, E.A., Hardersen, P.S., Bish, D.L., Bailey, D.T., Gaffey, M.J., Craig, M.A., 2009. Reflectance spectra of iron meteorites: Implications for spectral identification of their parent bodies. *Meteorit. Planet. Sci.*, submitted for publication.
- Davis, D.R., Farinella, P., Marzari, F., 1998. The missing Psyche family: Collisionally eroded or never formed? *Icarus* 137, 140–151.
- DeMeo, F.E., Binzel, R.P., Slivan, S.M., Bus, S.J., 2009. An extension of the Bus asteroid taxonomy into the near-infrared. *Icarus* 202, 160–180.
- Descamps, P., and 18 colleagues, 2008. New determination of the size and bulk density of the binary Asteroid 22 Kalliope from observations of mutual eclipses. *Icarus* 196, 578–600.
- Durech, J., and 41 colleagues, 2007. Physical models of ten asteroids from an observers' collaboration network. *Astron. Astrophys.* 465, 331–337.
- Farquhar, R., Kawaguchi, J., Russell, C., Schwehm, G., Veverka, J., Yeomans, D., 2002. Spacecraft exploration of asteroids: The 2001 perspective. In: Bottke, W.F., Jr., Cellino, A., Paolicchi, P., Binzel, R.P. (Eds.), *Asteroids III*. University of Arizona, Tucson, pp. 367–378.
- Fornasier, S., Clark, B.E., Dotto, E., Migliorini, A., Ockert-Bell, M., Barucci, M.A., 2009. Spectroscopic survey of M-type asteroids. *Icarus*, submitted for publication.
- Gaffey, M.J., 1976. Spectral reflectance characteristics of the meteorite classes. *J. Geophys. Res.* 81, 905–920.
- Gaffey, M.J., McCord, T.B., 1979. Mineralogical and petrological characterizations of asteroid surface materials. In: Gehrels, T. (Ed.), *Asteroids*. University of Arizona Press, Tucson, pp. 688–723.
- Gaffey, M.J., Burbine, T.H., Binzel, R.P., 1993. Asteroid spectroscopy: Progress and perspectives. *Meteoritics* 28, 161–187.
- Gaffey, M.J., Cloutis, E.A., Kelley, M.S., Reed, K.L., 2002. Mineralogy of asteroids. In: Bottke, W.F., Jr., Cellino, A., Paolicchi, P., Binzel, R.P. (Eds.), *Asteroids III*. University of Arizona, Tucson, pp. 183–204.
- Garvin, J.B., Head, J.W., Pettengill, G.H., Zisk, S.H., 1985. Venus global radar reflectivity and correlations with elevation. *J. Geophys. Res.* 90, 6859–6871.
- Greshake, A., Krot, A.N., Meibom, A., Weisberg, M.K., Zolensky, M.E., Keil, K., 2002. Heavily-hydrated lithic clasts in CH chondrites and the related metal-rich

- chondrites Queen Alexandra Range 94411 and Hammadah al Hamra 237. *Meteorit. Planet. Sci.* 37, 281–293.
- Haack, H., Rasmussen, K.L., Warren, P.H., 1990. Effects of regolith/megaregolith insulation on the cooling histories of differentiated asteroids. *J. Geophys. Res.* 95, 5111–5124.
- Hapke, B., 1981. Bidirectional reflectance spectroscopy. 1. Theory. *J. Geophys. Res.* 86, 3039–3054.
- Hardersen, P.S., Gaffey, M.J., Abell, P.A., 2005. Near-IR spectral evidence for the presence of iron-poor orthopyroxenes on the surfaces of six M-type asteroids. *Icarus* 175, 141–158.
- Harris, A.W., Young, J.W., 1983. Asteroid rotation. IV. 1979 Observations. *Icarus* 54, 59–109.
- Harris, A.W., Young, J.W., Dockweiler, t., Gibson, J., Poutanen, M., Bowell, E., 1992. Asteroid lightcurve observations from 1981. *Icarus* 95, 115–147.
- Hong, D.C., Quinn, P.V., Luding, S., 2001. Reverse Brazil nut problem: Competition between percolation and condensation. *Phys. Rev. Lett.* 86, 3423–3426.
- Hutchinson, R., 2004. *Meteorites: A Petrologic, Chemical, and Isotopic Synthesis*. Cambridge University Press, Cambridge, UK, 506 pp.
- Jones, T.D., Lebofsky, L.A., Lewis, J.S., Marley, M.S., 1990. The composition and origin of the C, P, and D asteroids: Water as a tracer of thermal evolution in the outer belt. *Icarus* 88, 172–192.
- Krot, A.N., Meibom, A., Weisberg, M.K., Keil, K., 2002. The CR chondrite clan: Implications for early Solar System processes. *Meteorit. Planet. Sci.* 37, 1451–1490.
- Lazzarin, M., Marchi, S., Moroz, L.V., Magrin, S., 2009. New visible spectra and mineralogical assessment of (21) Lutetia, a target of the Rosetta mission. *Astron. Astrophys.* 498, 307–311.
- Lebofsky, L., 1989. Wavelength dependence of IRAS asteroid diameters and albedos. *Icarus* 78, 355–362.
- Lupishko, D.F., 2006. On the bulk density and porosity of the M-type asteroid 16 Psyche. *Solar Syst. Res.* 40, 214–218.
- Lupishko, D.F., Belskaya, I.N., 1989. On the surface composition of the M-type asteroids. *Icarus* 78, 395–401.
- Magri, C., Ostro, S.J., Rosema, K.D., Thomas, M.L., Mitchell, D.L., Campbell, D.B., Chandler, J.F., Shapiro, I.L., Giorgini, J.D., Yeomans, D.K., 1999. Mainbelt asteroids: Results of Arecibo and Goldstone observations of 37 objects during 1980–1995. *Icarus* 140, 379–407.
- Magri, C., Consolmagno, G.J., Ostro, S.J., Benner, L.A.M., Beeny, B.R., 2001. Radar constraints on asteroid regolith properties using 433 Eros as ground truth. *Meteorit. Planet. Sci.* 36, 1697–1709.
- Magri, C., Nolan, M.C., Ostro, S.J., Giorgini, J.D., 2007. A radar survey of main-belt asteroids: Arecibo observations of 55 object during 1999–2003. *Icarus* 186, 126–151.
- Marchis, F., Descamps, P., Berthier, J., Emery, J.P. 2008. S/2008 (216) 1 and S/2008 (216) 2. *IAU Circular*, 8980.
- Margot, J.-L., Brown, M.E., 2003. A low-density M-type asteroid in the main belt. *Science* 300, 1939–1942.
- McKay, D.S., Swindle, T.D., Greenberg, R., 1989. Asteroidal regoliths: What we do not know. In: Binzel, R.P., Gehrels, T., Matthews, M.S. (Eds.), *Asteroids II*. University of Arizona, Tucson, pp. 617–642.
- Mitchell, D.L., Ostro, S.J., Rosema, K.D., Hudson, R.S., Campbell, D.B., Chandler, J.F., Shapiro, I.L., 1995. Radar observations of Asteroids 7 Iris, 9 Metis, 12 Victoria, 216 Kleopatra, and 654 Zelinda. *Icarus* 118, 105–131.
- Morrison, D., 1977. Asteroid sizes and albedos. *Icarus* 31, 185–220.
- Ockert-Bell, M.E., Clark, B.E., Shepard, M.K., Rivkin, A., Binzel, R., Thomas, C.A., DeMeo, F.E., Bus, S.J., Shah, S., 2008. Observations of X/M asteroids across multiple wavelengths. *Icarus* 195, 206–219.
- Ockert-Bell, M.E., Clark, B.E., Shepard, M.K., Isaacs, R.A., Cloutis, E., Bus, S.J., 2010. A synthesis of spectroscopic and radar evidence for the composition of Xc and Xk asteroids. *Icarus*, in preparation.
- Ostro, S.J., Campbell, D.B., Shapiro, I.L., 1985. Mainbelt asteroids: Dual polarization radar observations. *Science* 229, 442–446.
- Ostro, S.J., Campbell, D.B., Chandler, J.F., Hine, A.A., Hudson, R.S., Rosema, K.D., Shapiro, I.L., 1991. Asteroid 1986 DA: Radar evidence for a metallic composition. *Science* 252, 1399–1404.
- Ostro, S.J., Hudson, R.S., Nolan, M.C., Margot, J.-L., Scheeres, D.J., Campbell, D.B., Magri, C., Giorgini, J.D., Yeomans, D.K., 2000. Radar observations of Asteroid 216 Kleopatra. *Science* 288, 836–839.
- Ostro, S.J., Hudson, R.S., Benner, L.A.M., Giorgini, J.D., Magri, C., Margot, J.L., Nolan, M.C., 2002. Asteroid radar astronomy. In: Bottke, W.F., Jr., Cellino, A., Paolicchi, P., Binzel, R.P. (Eds.), *Asteroids III*. University of Arizona, Tucson, pp. 151–168.
- Pravec, P., Harris, A.W., 2007. Binary asteroid population. 1. Angular momentum content. *Icarus* 190, 250–259.
- Richardson, D.C., Leinhardt, Z.M., Melosh, H.J., Bottke, W.F., Asphaug, E., 2002. Gravitational aggregates: Evidence and evolution. In: Bottke, W.F., Jr., Cellino, A., Paolicchi, P., Binzel, R.P. (Eds.), *Asteroids III*. University of Arizona, Tucson, pp. 501–516.
- Rivkin, A.S., Howell, E.S., Britt, D.T., Lebofsky, L.A., Nolan, M.C., Branston, D.D., 1995. 3- μ m spectrophotometric survey of M and E-class asteroids. *Icarus* 117, 90–100.
- Rivkin, A.S., Howell, E.S., Lebofsky, L.A., Clark, B.E., Britt, D.T., 2000. The nature of M-class asteroids from 3- μ m observations. *Icarus* 145, 351–368.
- Rosato, A., Strandburg, K.J., Prinz, F., Swendsen, R.H., 1987. Why the Brazil nuts are on top: Size segregation of particulate matter by shaking. *Phys. Rev. Lett.* 58, 1038–1040.
- Scheeres, D.J., Durda, D.D., Geissler, P.E., 2002. The fate of asteroid ejecta. In: Bottke, W.F., Jr., Cellino, A., Paolicchi, P., Binzel, R.P. (Eds.), *Asteroids III*. University of Arizona, Tucson, pp. 527–544.
- Shepard, M.K., and 19 colleagues, 2008a. A radar survey of M- and X-class asteroids. *Icarus* 195, 184–205.
- Shepard, M.K., Kressler, K.M., Clark, B.E., Ockert-Bell, M.E., Nolan, M.C., Howell, E.S., Magri, C., Giorgini, J.D., Benner, L.A.M., Ostro, S.J., 2008b. Radar observations of E-class Asteroids 44 Nysa and 434 Hungaria. *Icarus* 195, 220–225.
- Stephens, R.D., Warner, B.D., Shepard, M.K., Harris, A.W., 2008. Lightcurve and radar observations and analysis of 11 Parthenope and 678 Fredegundis. *Bull. Am. Astron. Soc. Abstract* #28.16.
- Sullivan, R.J., Thomas, P.C., Murchie, S.L., Robinson, M.S., 2002. Asteroid geology from Galileo and NEAR Shoemaker data. In: Bottke, W.F., Jr., Cellino, A., Paolicchi, P., Binzel, R.P. (Eds.), *Asteroids III*. Springer, Berlin, pp. 331–350.
- Tanga, P., Hestroffer, D., Berthier, J., Cellino, A., Lattanzi, M.G., Di Martino, M., Zappala, V., 2001. HST/FGS observations of the Asteroid (216) Kleopatra. *Icarus* 153, 451–454.
- Tedesco, E.F., 1989. Asteroid magnitudes, UVB colors, and IRAS albedos and diameters. In: Binzel, R.P., Gehrels, T., Matthews, M.S. (Eds.), *Asteroids II*. University of Arizona, Tucson, pp. 1090–1138.
- Tedesco, E.F., Noah, P.V., Noah, M., 2002. The supplemental IRAS minor planet survey. *Astron. J.* 123, 1056–1085.
- Tholen, D., 1984. Asteroid taxonomy from cluster analysis of photometry. PhD thesis, University of Arizona, Tucson, 150pp.
- Timerson, B., and 46 colleagues, 2009. A trio of well-observed asteroid occultations in 2008. *Minor Planet Bull.* 36, 98–100.
- Torppa, J., Kaasalainen, M., Michalowski, T., Kwiatkowski, T., Kryszczyńska, A., Denchev, P., Kowalski, R., 2003. Shapes and rotational properties of thirty asteroids from photometric data. *Icarus* 164, 346–383.
- Tungalag, N., Shevchenko, V.G., Lupishko, D.F., 2003. Rotation parameters and shapes of 19 asteroids. Qualitative analysis and data interpretation. *Kinem. Phys. Celest. Bodies* 19, 272–279.
- Vernazza, P., Brunetto, R., Binzel, R.P., Perron, C., Fulvio, D., Strazzulla, G., Fulchignoni, M., 2009. Plausible parent bodies for enstatite chondrites and mesosiderites: Implications for Lutetia's fly-by. *Icarus* 202, 477–486.
- Vilas, F., 1994. A cheaper, faster, better way to detect water of hydration on Solar System bodies. *Icarus* 111, 456–467.
- Warner, B.D., Harris, A.W., Pravec, P., 2009a. The asteroid lightcurve database. *Icarus* 202, 134–146.
- Warner, B.D., Stephens, R.D., Harris, A.W., Shepard, M.K., 2009b. Coordinated lightcurve and radar observations of 110 Lydia and 135 Hertha. *Minor Planet Bull.* 36, 38–39.
- Zellner, B., Leake, M., Morrison, D., Williams, J.G., 1977. The E-asteroids and the origin of the enstatite chondrites. *Geochim. Cosmochim. Acta* 41, 1759–1767.